Design and Aerodynamic Analysis of Continuous Mold-line link flap

Aditya Narkhede

Thesis submitted to the faculty of the Virginia Polytechnic Institute and State University in partial fulfillment of the requirements for the degree of

Master of Science
In
Aerospace Engineering

Michael K Philen
William J Devenport
Mayuresh J Patil

July 15th, 2021
Blacksburg, Virginia

Keywords: Computational Fluid Dynamics, Viscous flow, Inviscid flow, Aerodynamics, Continuous mold-line link flap, Conventional hinged flap, Parabolic flap.

Design and Aerodynamic Analysis of Continuous Mold-line link flap

Aditya Narkhede

ABSTRACT

Flaps used in modern aircraft are known to produce high intensity noise. Their blunt side edges produce vorticial wakes which are the main contributors to the noise generated. To avoid this issue, a concept called continuous mold-line (CML) link flap has been studied rigorously for its impact on the acoustic behavior of the wing. It has been found that eliminating the blunt side tips with a continuous mold-line reduces the noise generated by the wing drastically. However, very few studies have been conducted to understand the effects of the shape of the mold-line on its aerodynamic characteristics. Therefore, the overall objective of this research is to investigate the effects of shape and geometry on the aerodynamics. First the shape of the continuous mold-line is parametrized using a hyperbolic tangent curve. Then, using ANSYS Fluent a computational model is developed to calculate the lift and drag generated by different CML configurations. Both, inviscid and viscous studies are performed using the Fluent's pressure-based solver. The effects of span and slope at the mid-point of the transition zone are discussed. It was found that the slope at mid-point of the transition zone does not affect the overall lift generated by the wing. Also, increasing the span of the transition zone initially increases the drag and begins to decrease at different span lengths. Overall, it was found that the aerodynamic characteristics (such as lift, drag and efficiency) of the CML wing is better than the conventional blunt tip hinged flap.

Design and Aerodynamic Analysis of Continuous Mold-line link flap

Aditya Narkhede

GENERAL AUDIENCE ABSTRACT

Flaps used in modern aircraft are known to produce high-intensity noise. One of the main contributors to the high-intensity noise is the blunt side edges of the wing's flap. To eliminate the noise produced by the flaps, researchers have come up with a concept called continuous mold-line (CML) link flap. In this concept, we join the flap side edge with the main wing and thus remove the side edges. Studies undertaken till now have mainly focused on the acoustic aspects of the CML wing. Hence, this study focuses on the effect the mold-line shape has on the wing's aerodynamic behavior. The study first discusses a parametric curve that will be used to define the shape of the CML region of the wing. Then, the study calculates the aerodynamic characteristics, such as lift and drag generated by the wing, using the commercial software ANSYS FLUENT. The results obtained by changing the slope at the mid-point and length of the CML region are discussed. Finally, the study presented also compares the aerodynamic characteristics (such as lift, drag, and efficiency) of the CML wing are better than the conventional blunt tip hinged flap.

Table of Contents

List of Figures

1. Introduction

1.1. General

Over the years, as the population continues to increase, airports that used to be far away from residential areas have now come to be a part of them. This movement of civilization towards airports has serious health impacts, especially on those who reside nearby. One of them is the noise that airports create. An aircraft that approaching or taking off from an airport can produce noise levels that are close to the human threshold for eardrum rupture. Such drastic impacts on human health have motivated researchers to look for alternatives that produce a quieter aircraft without losing aerodynamic efficiency.

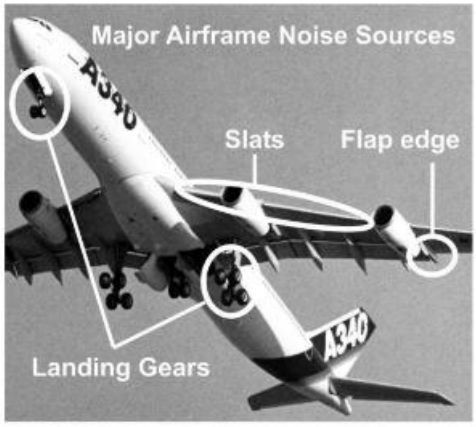

Figure 1. Airframe major noise sources.

During the aircraft approach, the engine is idle, and the high-lift devices and landing gears are fully deployed. In such a configuration the airframe noise is the dominant source of noise [1]. Dobrzynski [2] provided a brief history of research – both experimental and computational – conducted to identify airframe noise sources, their mechanisms, and technologies developed to mitigate the noise levels. Through his study, he noted that the typical rank of priority of airframe noise sources were landing gears, slotted flaps, flap and slat side edge, flap and slat

tracks, and component interactions are the major airframe noise sources. Considerable research is being undertaken to get a better understanding of each source. But, for this study, we will not dwell further into each noise source, instead, we will be focusing on flap side edges as it is one of the major sources of airframe noise.

1.2. Flow over the flap side edge

In order to understand ways to reduce the noise produced by flap side edges, we first need to look at the mechanisms that produce the noise. Over the years, a great deal of experimental and computational effort has been expended in trying to understand these mechanisms and to derive empirical relations to quantify their effects.

Using a 1:10 scaled model of an Airbus-type high-lift device and employing high-resolution acoustic mirror measurements, Dobrzynski, Nagakura, Gehlhar and Buschbaum [3] studied the mechanisms that produce the slat and flap-side edge noise. They identified that slats were dominant in the lower frequency spectra whereas flap-side edges were a stronger source for high frequencies. For flap-side edge, the noise source mechanism varied with velocity and angle of attack. For mid-range frequencies, it was identified that unsteady flow and flap interaction produced a dipole type noise source mechanism. Whereas for high frequencies, the vortex leaving the side-edge proved to be the dominant noise source. Apart from this, they also studied some preliminary noise-reducing components which, on average, provided about 4dB of noise reduction.

As a part of NASA Langley and Ames Research Center's program to get a deeper understanding of fundamental mechanisms of airframe noise generation, Radeztsky, Singer and Khorrami [4] studied the behavior of the flow leaving an unswept Fowler flap wing. They found that beginning at the separation two vortices are formed, one on the lower portion of the flap side edge and the other on the upper surface. The flap side vortex is much stronger

compared to the upper surface vortex and around the mid-chord of the flap, these two vortices merge into one. The evolution of the vortical structures can be seen in Figure 2 and Figure 3. At higher flap deflections vortex bursting was also observed which was thought to be one of the reasons for high noise levels at these conditions. These results were consistent with those obtained through unsteady Navier-Stokes calculations, pressure distribution data, and those published in Storms, Takahashi and Ross [5].

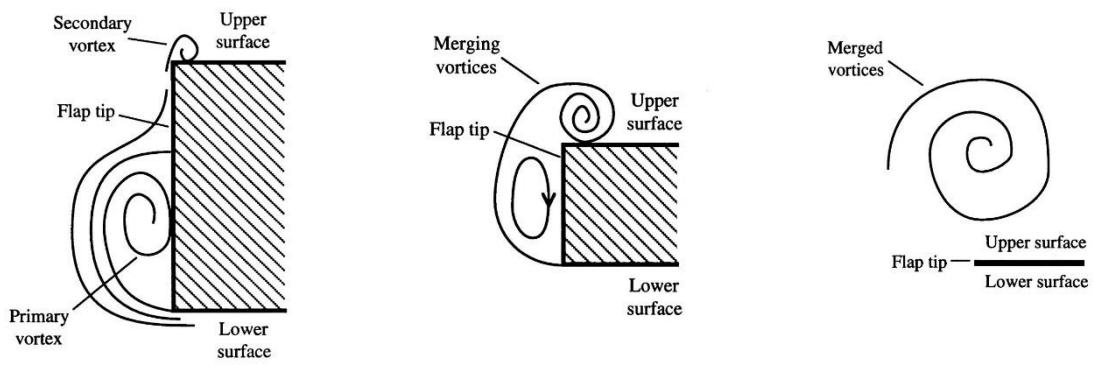

$x/c = 0.1$ $x/c = 0.18$ $x/c = 0.3$

Figure 2. Evolution of vortex structures near flap side edge – Storms, Takahashi and Ross [5].

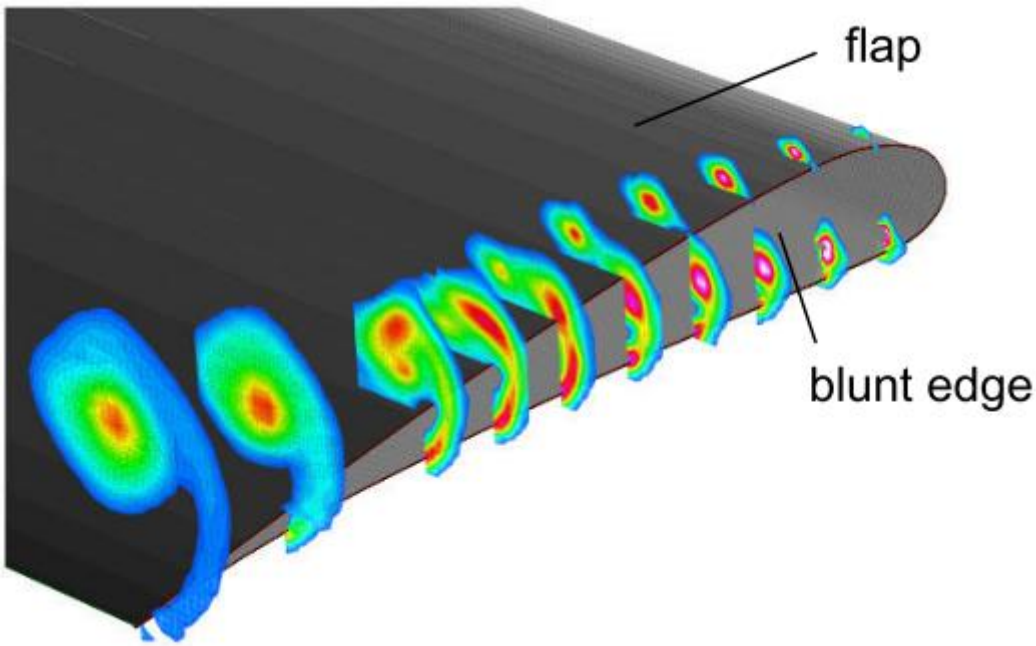

Figure 3. 5 hole probe measurements of axial vorticity contours for a flap deflection of 29° – Hutcheson, Brooks and Humphreys Jr [1].

From the data presented in Dobrzynski [2], Dobrzynski, Nagakura, Gehlhar and Buschbaum [3], Radeztsky, Singer and Khorrami [4], and Storms, Takahashi and Ross [5], we now know that the noise produced by these vortical structures is a key component of overall noise generated by the flap side edge. Hence, to reduce the noise from the side edges we need to find ways to suppress or eliminate these vortices. Various technologies like porous side edges and add-on side edge fences have been proposed for suppressing the vortex structures. A more radical approach is to eliminate the flap side edge altogether using the so-called continuous mold line technology [2]. This was first suggested by Storms, Jaeger, Hayes and Soderman [6] but, was later on studied in more detail by Hutcheson, Brooks and Humphreys Jr [1], Streett, Casper, Lockard, Khorrami, Stoker, Elkoby, Wenneman, Underbrink, Wenneman and Underbrink [7], and Kamliya Jawahar, Zang and Azarpeyvand [8]. In this study we will be exploring the benefits of using continuous mold line technology and a detailed review of the research done till now is presented in the next section.

1.3. Continuous mold line technology

Storms, Jaeger, Hayes and Soderman [6] investigated the aero-acoustic and aerodynamic effects of introducing continuous mold line technology (CMT) to a standard hinged flap. At that time blended wing-body aircraft were prime candidates for subsonic aircraft designs because of their increased aerodynamic efficiency for large aircraft. Concepts like blending the passenger cabin to the wing root led to a decrease in overall wing loading, and because of this decrease high lift devices were not required as classical hinged flaps provided the required wing loading. Hence, they decided to use an airfoil with a hinged flap. For their experiments, they used two configurations of the NACA 63_2-215 Mod B flap. The first configuration had a 30% chord half span hinged flap and in the second configuration, CML replaced 29% of the span – both of which are shown in Figure 4. These models were then tested at NASA Ames 7 ft by 10 ft closed wind tunnel. The acoustic data was obtained using a phased microphone array

mounted on the wing's pressure side. The results were presented for a flap deflection of 39° and freestream velocity corresponding to Mach 0.22. Their aero-acoustic study found that hinged flap configuration was about 6 - 8dB quieter compared to the Fowler flap configuration that is used in practice. The reason for this lower noise level was stated to be the lower lifting loads for hinged flaps. Lower wing loading meant that the flow had less energy to contribute to the wingtip vortices and hence produced lower noise. Unfortunately, their experimental setup was not able to quantify the CMT noise levels as the noise generated by the CMT configuration was less than the background noise of the wind tunnel. However, they estimated that CMT was about 6dB quieter compared to the hinged flap.

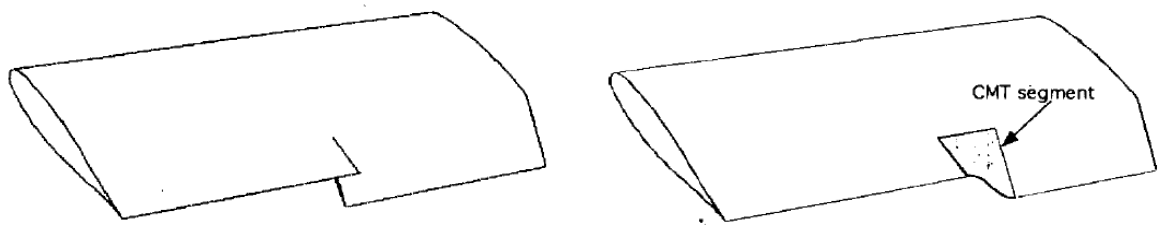

(a) Hinged flap configuration. (b) Hinged flap configuration with CMT.

Figure 4. NACA 63_2-215 Mod B flap configurations used in [6].

Their aerodynamic study on the other side portrayed a different picture. Relative to the hinged flap the lift distribution over the span for CMT was on the lower side and hence produced a lower coefficient of lift. It was noted that the decrease in the lift for CMT was because it was replacing 29% of the flap span. By replacing a part of a fully deployed flap span with CMT a section that was supposed to be at flap deflection angle was now at a lower deflection which led to a decrease in its contribution to spanwise lift. If instead, part of the main stationary airfoil was replaced by CMT then there could be an increase in lift performance. Hence, the location of CMT is of utmost importance to increase the aerodynamic efficiency of the wing.

A similar study for evaluating the aero-acoustic performance of leading-edge slats, slat tip, and flap side edges was done by Streett, Casper, Lockard, Khorrami, Stoker, Elkoby, Wenneman, Underbrink, Wenneman and Underbrink [7]. But, for their study, they used a swept multi-element wing which is traditionally used in commercial aircraft. A microphone-phased array system was mounted on the walls of a closed section wind tunnel on the pressure side of the model. Using the microphone-phased array system, they were able to measure the noise generated by the Continuous Mold-line Link (CML) flap. By comparing the peak SPL data for CML flap with a part span flap, they found that CML reduced the radiated sound by about 5-15 dB for all frequencies over 2.5kHz. Although their aero-acoustic data gave such crucial details about CML flap performance, due to the lack of availability of data for part span flaps, their aerodynamic results do not give good insights regarding CML flap's aerodynamic performance. However, they speculated that adding CML for a distance of less than 2/3-chord in the span should have little to no effect on stall characteristics of the wing because slats present in the outer part of the wing are primarily responsible for the stall.

Hutcheson, Brooks and Humphreys Jr [1] investigated the CML flap configuration to locate the noise sources, determine their strength, and understand the directivity of the radiated sound. They conducted their studies in the Quite Flow Facility at NASA Langley Research Center. A medium directional array of microphones was used to acquire the acoustic data and the Deconvolution Approach for Mapping of Acoustic Sources method was employed to determine the strength and location of the noise sources. Additionally, they also used the Coherent Output Power approach to correlate the unsteady pressure surface measurements to the acoustic data which gave the acoustic source distribution over the trailing edge region of the CML flap. Data was acquired for two configurations of CML flap with NACA 63_2-215 airfoil sections. The two configurations differed in flap deflection angle, one was at 29° and the other at 39°. The wings were placed in the open jet nozzle at an angle of 16°. The results showed that, compared

to blunt flaps, the CML flap generated 5-17 dB lower sound output. The level of noise produced by the CML flap was dependent on the flap deflection and freestream Mach number. The largest reduction in noise level was observed for the 39° flap configuration. Further, the COP method's results identified that between 1 and 3.5 kHz frequency range, the noise sources were distributed along the CML trailing edge region, and the location of strongest radiation was different on the pressure and suction sides.

The above-presented research supports the fact that replacing the blunt flap side edges with a seamless continuous spanwise transition provides acoustic benefits. It distributes the energy of flap tip vortices over the span of the wing which leads to about 10dB lower sound output. In addition to the acoustic benefits of the CML, the CML can also improve the aerodynamics of the airfoil although not as much research has been published on the topic.

Pankonien and Inman [9] sought to answer this very question. In their investigation, they have compared the aerodynamic performance of a spanwise morphing trailing edge to a blunt tip flap's performance. They have achieved spanwise variation using alternating active and passive sections (see Figure 5). The passive sections were made up of elastomeric honeycomb bonded to a pre-strained skin which would stretch between active sections and resist the aerodynamic loads. The active sections employed the cascading bimorph concept to bend the trailing edge of the wing section and obtain a smooth chordwise camber variation. Since they were testing this concept for low-speed UAV applications, the airfoil section adopted was NACA 0012. The two wings were tested in the wind tunnel at the University of Michigan in a free stream velocity of 10 m/s and angles of attack 5° and 10°, representing attached and separated flows, respectively. The results showed that for the attached flow, the morphing wing was able to achieve almost similar change in the lift as seen for blunt flap wing but with less drag. For attached flows, they also observed that, by increasing the span of the blunt flap wing the relative effect of the inboard vortex decreased. This resulted in improved relative performance. In

contrast, for separated flow, increasing the flap span simply increased drag. These effects were not present for the morphed wing, highlighting the benefits of using a smooth continuous surface.

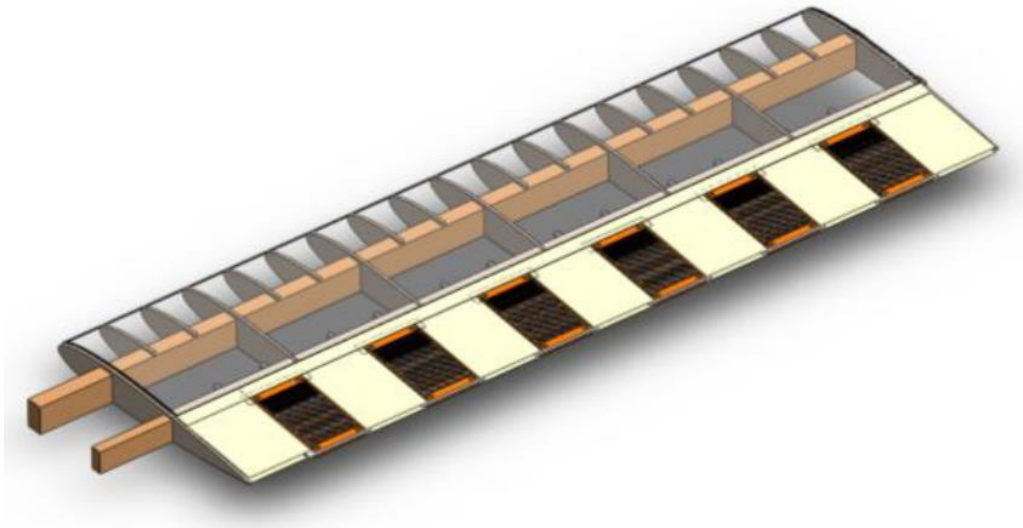

Figure 5. The modular design of alternating active and passive sections for NACA 0012 airfoil [9].

Further, Ninian and Dakka [10] also studied the effects of adding a seamless transition between the flap and stationary wing. They conducted both experimental and computational studies. The experiments were conducted using two wings, one with a conventional blunt side edge flap and one with an optimized continuous transition. Whereas the computational study was conducted on three different configurations of the flap: (1) the conventional flap; (2) a flap with the initial design for the seamless transition; (3) the optimized continuous mold-line link flap. All three geometries had the same flap span and section profile. All three geometries had the same flap span and section profile. Their results suggest that both the initial design and optimized design showed better aerodynamic efficiency for various angles of attack compared to the conventional flap. The computational study revealed that due to the elimination of gaps

between the flap and the stationary wing surface, the pressure on the lower surface of the wing increased and the pressure distribution over the whole wing surface was smoother. The initial and optimized wings were also able to reduce the size of the side tip vortex and delay their formation in the wake region, which resulted in a reduction of pressure drag.

A similar study conducted by Abdessemed, Yao, Bouferrouk and Narayan [11] compared the aerodynamic efficiency of a statically morphed wing and dynamic morphing wing to the conventional blunt flapped wing. The morphed wings had seamless spanwise transition like the ones presented in previous papers. A Computational Fluid Dynamics (CFD) model with $k - \omega$ SST turbulence equations was used to obtain the co-efficient of lift and drag. The three wings were tested for $Re = 0.62 \times 10^6$ and $Ma = 0.115$. Their results showed that for lower angles of attack the statically morphed wing had almost 40% better aerodynamic efficiency compared to the conventional flap. However, at higher angles, the performance of the continuous mold-line link deteriorated a bit and that the conventional flap showed consistent performance. Also, due to unsteady effects coming into the picture for dynamically morphing continuous mold-line link, the overall efficiency observed was less compared to its statically morphed counterpart.

The research listed above highlights the benefits of using a continuous mold-line link flap over conventional hinged flaps. These benefits are not only limited to aeroacoustics but also extend to the aerodynamic aspects of the wing. But, till now we have seen the aerodynamic benefits of a linear continuous mold-line. From the research conducted till now, it is evident that the lift, drag, and pressure distributions depend on the seamless transition. However, little research has been performed on investigating the effects of the shape of the transition region.

Kamliya Jawahar, Zang and Azarpeyvand [8] considered 5 different Spanwise Morphing (SPM) shapes (see Figure 6). Out of the five SPM configurations, SPM case 1 and SPM case

5 have the most extreme change in spanwise slope. For SPM case 1 this change in slope causes a reduction in the area of the deflected trailing edge. Whereas for SPM case 5, it increases the area of the deflected trailing edge. The SPM-baseline mentioned in Figure 6, represents a discontinuous morphing angle transition at the mid-span location.

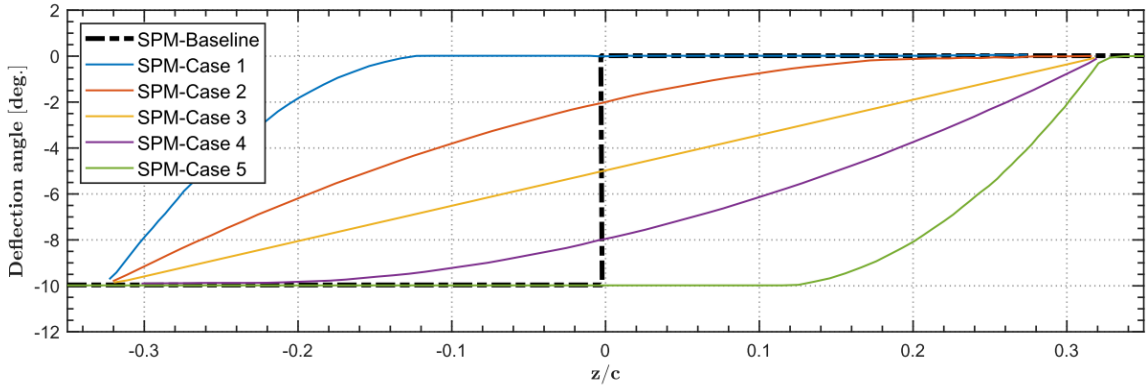

Figure 6. Trailing edge profiles of various spanwise morphing configurations tested [8].

The SPM configurations were tested at the University of Bristol open-jet wind tunnel under the free stream conditions of $U_\infty = 20\, m/s$ and $Re_c = 2.6 \times 10^5$ with the flap deflection angle set to 10°. Aerodynamic lift and drag measurements were carried out using the hot-wire anemometry technique. The aerodynamic results showed that the values of lift and drag depend heavily on the shape of the spanwise morphing. It was found that the best overall aerodynamic performance was depicted by the SPM case 3 configuration which denotes a linear spanwise variation. Even the aeroacoustics results showed the same behavior.

From the research presented till now, it is quite evident that the continuous mold-line link concept holds merit and can be utilized to improve the efficiency of an air vehicle. The fact that its performance is highly dependent on its shape adds an extra dimension to its design process. The objective of this study is to further look into this aspect of the continuous mold-

line link flap and to define a parametrizable curve that describes the trailing edge profile which can be used in future multi-disciplinary optimization of the wing.

1.4. The rationale behind using parabolic flaps.

Traditional hinged flaps, due to their sudden change in shape from the stationary part of the wing to the flap, have an inherent cavity-type acoustic source present [12]. This source can be eliminated using a smooth transition which can be obtained by changing the wings camber profile in the flap region. Kamliya Jawahar, Ai and Azarpeyvand [12] found that for the same flap deflection, a highly cambered airfoil produced higher lift compared to an airfoil with a conventional hinged flap. Highly cambered profiles did show a decrease in aerodynamic efficiency but, the reduction was almost insignificant. It was also noted that the highly cambered profile delayed the separation point compared to the hinged flap.

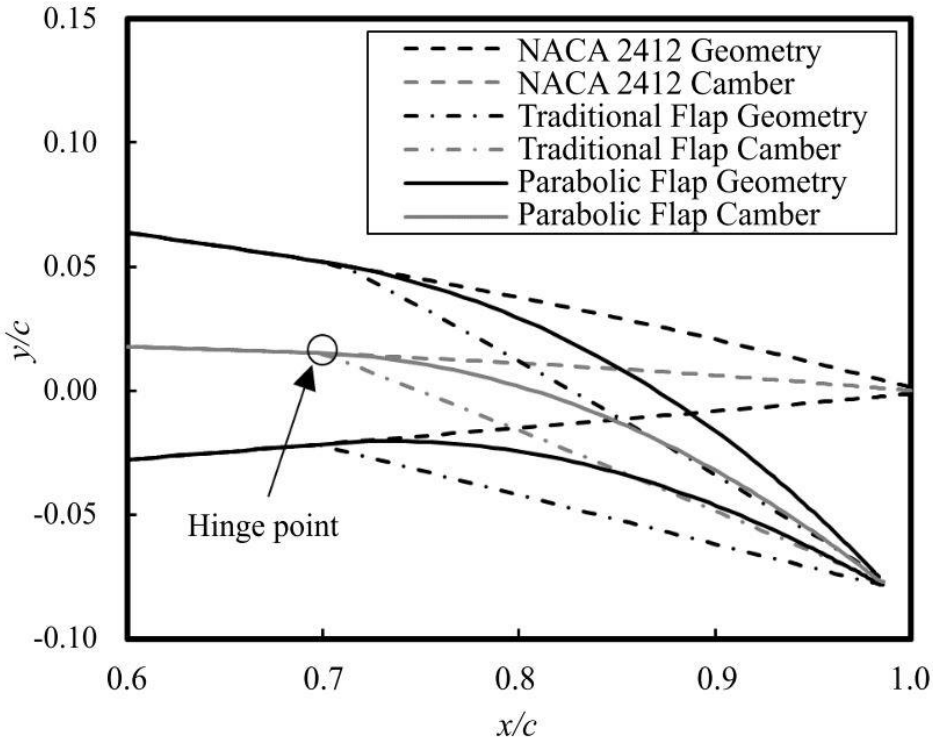

Figure 7. Airfoil flap geometry and camber line for NACA 2412 with different flap definitions [13].

Hunsaker, Reid and Joo [13] developed their definition for the camber line of parabolic profile such that the overall flap length remains unchanged. They conducted an ideal aerodynamic analysis and obtained the analytic solutions for the aerodynamic coefficients using the thin airfoil theory. Their study found that for a parabolic flap the aerodynamic efficiency was typically 33% to 50% higher than that of a hinged flap. The increase depended on the flap-chord ratio – larger flap-chord ratios producing larger gains. Additionally, the parabolic flap was able to achieve the same aerodynamic efficiency as the hinged flap for about 65% to 80% flap deflections. Again, the amount of flap deflection depended on the flap-chord ratio.

Over the years, myriad studies have been conducted to understand the flow behavior and improve the aerodynamic efficiency of the morphing flap. A historical overview of these studies has been documented in Barbarino, Bilgen, Ajaj, Friswell and Inman [14]. With the studies presented above, it is quite evident that morphed trailing edges have aerodynamic benefits over the traditional hinged flaps. Hence, in our study, we will be taking into consideration the combined effects of spanwise morphing and parabolic flaps. For the geometric definition of the parabolic flap, we will be using the method developed in [13].

1.5. Motivation and objectives.

The continuous mold-line link technology has proven aero-acoustic and aerodynamic benefits, but there seems to be a lack of information regarding the effects its shape and size has on these quantities. This study aims to delve deeper into this aspect of continuous mold-line link and understand the influence shape and size have on aerodynamic quantities like lift and drag.

The study also aims to define a parametric curve that describes the spanwise trailing edge profile of the region that joins the flap to the stationary part of the wing. This curve will be defined in such a way that it has controllable parameters which can be used to optimize the shape of the seamless region such that we have improved aerodynamic efficiency.

A computational investigation of a wing with parabolic flap and continuous mold-line link will be done using two models, a pressure-based inviscid model, and a pressure-based $k - \omega$ SST turbulence model. We will be looking at the aerodynamic performance of the wing at low angles of attack. The results obtained from both of these models will be compared to the aerodynamic quantities of a wing comprised of a parabolic flap and blunt flap side edge.

1.6. Chapter overview

In the subsequent chapters, first, we will look at the parametric curve definition of the spanwise trailing edge, pressure-based inviscid flow theory and equations, pressure-based viscous $k - \omega$ SST turbulence model's theory, and equations, and the computational setup of ANSYS. In Chapter 3 we will first verify that the ANSYS models used for this study work by comparing to reported results in the literature. This will be done by running the model first for a rectangular NACA 0012 wing, results for which are easily available in past research. Finally, in Chapter 4 we will discuss the conclusions of the study and future scope.

2. Theory and Computational Setup

This chapter deals with the model setup and the theory behind the methods used to determine the aerodynamic coefficients. First, we will discuss the mathematical definition of the parametric curve used to define the spanwise transition from the flap to the stationary wing. Then, a brief review of the pressure based inviscid and viscous $k-\omega$ SST equations is presented. And lastly, we will see how the ANSYS solver is setup to output the necessary aerodynamic values.

2.1. Parametric spanwise trailing edge

The issue at hand is to join the blunt side edge of the flap to main stationary wing (see Figure 8 and Figure 9) using a continuous function that would remain continuous even if we change certain parameters like flap deflection, span of transition zone, slope of the continuous curve etc.

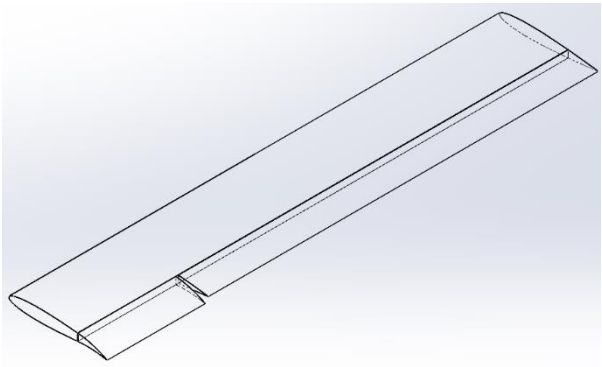

Figure 8. Conventional blunt side edge flapped wing with a parabolic flap.

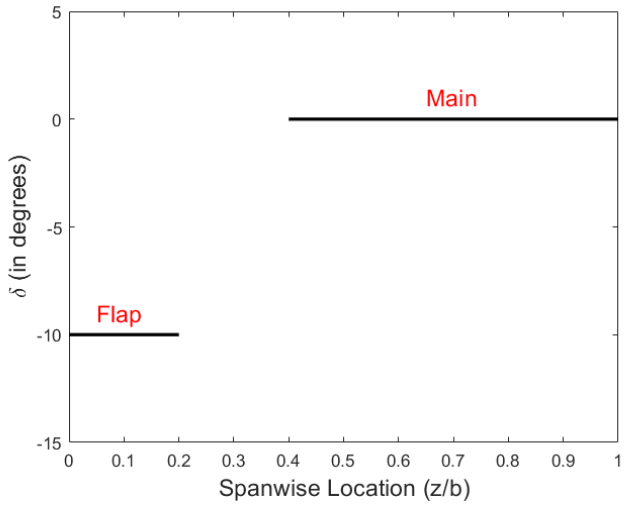

Figure 9. Trailing edge profile of the conventional flapped wing.

In our study we will be using a hyperbolic tangent profile – of the form Equation (2.1) – to join the flap to the main airfoil. The profile is defined parametrically using the variable 't' which depends on the spanwise location of the side edge of the flap (z_{flap}) and the span the of the transition zone (s). The parametric curve calculates the chordwise deflection (y in meters) of a section at a particular spanwise location (z in meters).

$$y(t) = a\tanh(bt + c) + d \qquad where\ \ t = \frac{z - z_{flap}}{s} \tag{2.1}$$

The constants a, b, c and d are determined by imposing the continuity conditions at the side tip of the flap and the main airfoil. Additionally, the deflection at the half span of the transition zone is fixed to the average of flap and main wing tip deflections, and the slope at the half span of the transition zone (δ_{mid}) is set to vary according to requirement. The mathematically form of these conditions is mentioned below in Equations (2.2) through (2.5).

$$y(0) = y_{flap} = a\tanh(c) + d \tag{2.2}$$

$$y(1) = y_{main} = a\tanh(b + c) + d \tag{2.3}$$

$$y(^1/_2) = \frac{y_{flap} + y_{main}}{2} = a \tanh\left(\frac{b}{2} + c\right) + d \tag{2.4}$$

$$\left.\frac{\partial y}{\partial z}\right|_{t=^1/_2} = \delta_{mid} = \frac{ba}{s} \operatorname{sech}^2\left(\frac{b}{2} + c\right) \tag{2.5}$$

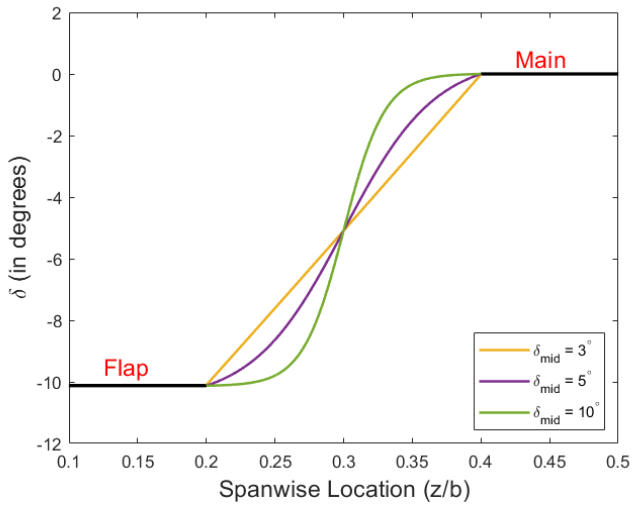

Figure 10. Trailing edge profile of a continuous mold-line link flap with the seamless transition parametrized by a hyperbolic tangent curve.

The benefits of using this parametric definition of the seamless transition are that:

- The profile obtained is continuous.
- The shape of the transition profile is controllable using the geometric parameters y_{flap}, y_{main}, δ_{mid}, and s.
- The solution for nonlinear system given in Equations (2.2) through (2.5) exists only for a certain value of δ_{mid}. Hence, it indirectly bounds the feasible values for δ_{mid}. The lower bound for δ_{mid} is the linear slope that joins the flap to the main wing (for Figure 10 the linear slope is 3°) and the upper bound depends on the values of y_{flap}, y_{main}, and s.

2.2. Inviscid flow equations

For a body of density ρ moving with a velocity $\vec{v}_b$ in a Newtonian fluid which has a velocity field $\vec{v}$, the equations of conservation of mass, momentum and energy (neglecting body forces) in their differential form are listed in Equations (2.6), (2.7), and (2.8) respectively.

$$\frac{\partial \rho}{\partial t} + \vec{\nabla} \cdot \rho(\vec{v} - \vec{v}_b) = 0 \tag{2.6}$$

$$\frac{\partial \rho \vec{v}}{\partial t} + \vec{\nabla} \cdot [\rho \vec{v}(\vec{v} - \vec{v}_b)] = -\vec{\nabla} p + \vec{\nabla} \cdot \vec{\vec{\tau}} + \rho \vec{b} \tag{2.7}$$

$$\frac{\partial \rho e}{\partial t} + \vec{\nabla} \cdot (\rho e \vec{v}) = -\vec{\nabla} \cdot (p\vec{v}) + \vec{\nabla} \cdot (\vec{\vec{\tau}} \cdot \vec{v}) + \vec{\nabla} \cdot (k\vec{\nabla} T) \tag{2.8}$$

where, p is the static pressure, $\vec{\vec{\tau}}$ is the viscous stress tensor, $\vec{b}$ is the body force vector, e denotes the total energy, and $k\vec{\nabla}T$ term represents the heat conduction, respectively. For our analysis we will not need the energy equation. Also, in our model we do not have any body forces – like gravity, electromagnetic, Coriolis etc. – and our wing model remains stationary in the fluid field. Additionally, since we are testing our wing model at low Mach numbers, we can assume that the density remains constant throughout the fluid domain. Hence, the equations reduce to:

$$\vec{\nabla} \cdot \vec{v} = 0 \tag{2.9}$$

$$\frac{\partial \rho \vec{v}}{\partial t} + \vec{\nabla} \cdot (\rho \vec{v} \vec{v}) = -\vec{\nabla} p + \vec{\nabla} \cdot \vec{\vec{\tau}} \tag{2.10}$$

The viscous stress tensor $\vec{\vec{\tau}}$ for a Newtonian fluid is given by:

$$\vec{\vec{\tau}} = \mu \left(\vec{\nabla} \vec{v} + \left(\vec{\nabla} \vec{v} \right)^T \right) - \frac{2}{3} \mu (\vec{\nabla} \cdot \vec{v}) \vec{\vec{I}} \tag{2.11}$$

where, μ is the fluid's absolute viscosity and $\vec{\vec{I}}$ is the identity tensor.

Now, let us first non-dimensionalize the primary variables as shown in Equations (2.12) through (2.15).

$$\vec{v}^* = \frac{\vec{v}}{U_\infty} \tag{2.12}$$

$$\vec{r}^* = \frac{\vec{r}}{c} \tag{2.13}$$

$$p^* = \frac{p}{\rho U_\infty^2} \tag{2.14}$$

$$t^* = \frac{tU_\infty}{c} \tag{2.15}$$

where, U_∞ is the freestream velocity and c is the chord length of the wing model. Introducing the non-dimensional parameters to Equation (2.10), then substituting Equation (2.11) in (2.10) and finally rearranging a few terms, the new non-dimensional conservation equations obtained are given by Equations (2.16) and (2.17).

$$\vec{\nabla} \cdot \vec{v}^* = 0 \tag{2.16}$$

$$\frac{\partial \vec{v}^*}{\partial t^*} + \vec{\nabla}^* \cdot (\vec{v}^* \vec{v}^*) = -\vec{\nabla} p^* + \frac{1}{Re_c} \nabla^2 \vec{v}^* \tag{2.17}$$

where Re_c denotes the chordwise Reynolds number. Now, for an inviscid and steady flow the unsteady term and the viscous term in the Equation (2.17) can be dropped as they amount to zero. Hence, for an inviscid and steady fluid flow the equations are further reduced to:

$$\vec{\nabla} \cdot \vec{v}^* = 0 \tag{2.18}$$

$$\vec{\nabla}^* \cdot (\vec{v}^* \vec{v}^*) = -\vec{\nabla} p^* \tag{2.19}$$

In our analysis we will be utilizing ANSYS' pressure-based solver for our incompressible and inviscid fluid flow. In this pressure-based solver, an elliptic Poisson's type equation is derived by substituting the velocities obtained from discretized momentum equations into the discretized continuity equation. This elliptic Poisson's type equation obtained is called the pressure equation, which is then used to solve for pressure.

Hence, at each iteration ANSYS first calculates a prediction for velocity field ($\vec{\tilde{v}}$) using the discretized momentum equation and ignoring the pressure variation. Based on this prediction the pressure equation is solved to determine the pressure distribution in the fluid domain. Once we have the pressure distribution the velocity field is corrected using the complete discretized momentum equation. This process is repeated till convergence is achieved.

2.3. Viscous $k - \omega$ SST equations

The viscous $k - \omega$ SST model was developed by Menter [15] to effectively utilize the robust and accurate formulation of standard $k - \omega$ model in the near wall region and take advantage of free stream independence of the $k - \epsilon$ model. First the $k - \epsilon$ is reformulated to match the standard $k - \omega$ model. Then, a blending function is multiplied with the original model and with the transformed model. The blending function controls which model the solver would use. In the near wall region, it takes the value of one, and hence activates the standard $k - \omega$ model. Outside of the boundary layer it takes the value of zero which activates the transformed $k - \epsilon$ model.

A similar blending function is also applied to the shear-stress transport (SST) equations to recover the original eddy viscosity formulation in the free shear layers.

In addition to Equations (2.9) and (2.10), we would also need transport equations for turbulence kinetic energy (k) and specific dissipation rate (ω). These equations are listed below in Equations (2.20) and (2.21).

$$\frac{\partial(\rho k)}{\partial t} + \vec{\nabla} \cdot (\rho k \vec{v}) = \vec{\nabla} \cdot \left(\Gamma_k \vec{\nabla} k\right) + \tilde{G}_k - Y_k + S_k \tag{2.20}$$

$$\frac{\partial(\rho \omega)}{\partial t} + \vec{\nabla} \cdot (\rho \omega \vec{v}) = \vec{\nabla} \cdot \left(\Gamma_\omega \vec{\nabla} \omega\right) + G_\omega - Y_\omega + S_\omega + D_\omega \tag{2.21}$$

In the equations above, Γ is the effective diffusivity term, $\tilde{G}_k$ is the turbulence kinetic energy produced due to mean velocity gradients, G_ω is the amount of ω generated, D_ω is the additional cross diffusion term, Y_ω and Y_k denote the dissipation of ω and k due to turbulence, and S represents the user defined source term.

For a steady state simulation, the unsteady terms in Equations (2.20) and (2.21) can be dropped and the resulting equations obtained are:

$$\vec{\nabla} \cdot (\rho k \vec{v}) = \vec{\nabla} \cdot \left(\Gamma_k \vec{\nabla} k\right) + \tilde{G}_k - Y_k + S_k \tag{2.22}$$

$$\vec{\nabla} \cdot (\rho \omega \vec{v}) = \vec{\nabla} \cdot \left(\Gamma_\omega \vec{\nabla} \omega\right) + G_\omega - Y_\omega + S_\omega + D_\omega \tag{2.23}$$

As the Equations (2.9), (2.10), (2.22), and (2.23) are coupled, ANSYS solves for pressure, velocity, turbulent kinetic energy, and specific dissipation rate iteratively till either continuity or momentum equations are converged.

2.4. ANSYS setup

To run a CFD simulation in ANSYS we need a fluid domain with the model, mesh, and a solver setup according to the freestream conditions and type of solution process. In our analysis, the geometry of the wing surface changes as we vary the slope and span of the transition zone. Additionally, it it's difficult to get a perfect hyperbolic tangent profile in CAD softwares like SolidWorks. Also, since the flap chord is a fraction of the wing's chord, in the transition region a portion of the wing remains stationary whereas the flap region transitions from flap to the

main wing (see Figure 11). To build the wing surface correctly, we will use SolidWorks ability to take coordinates of a curve from the user.

A MATLAB script will generate the coordinate data file based on the parameters like flap deflection, flap chord, transition zone span, slope of the transition zone, and the airfoil profile. This coordinate data file is then passed to SolidWorks which creates the wing body and stores it as an IGES file. The process is repeated for the number of wing bodies we have. Unfortunately, for now, this process is done manually. In future, we can automate this process and perform aerodynamic optimization in MATLAB.

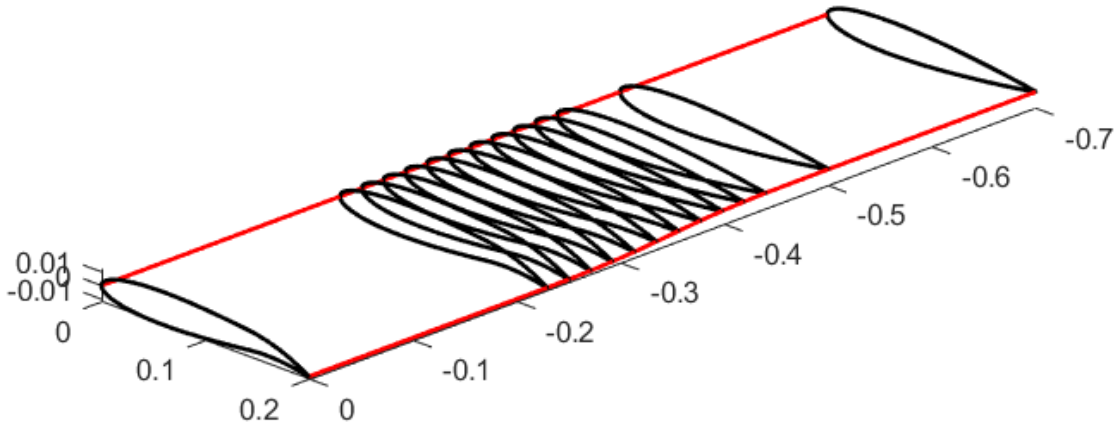

(a) Wing rib sections for which MATLAB generates coordinates.

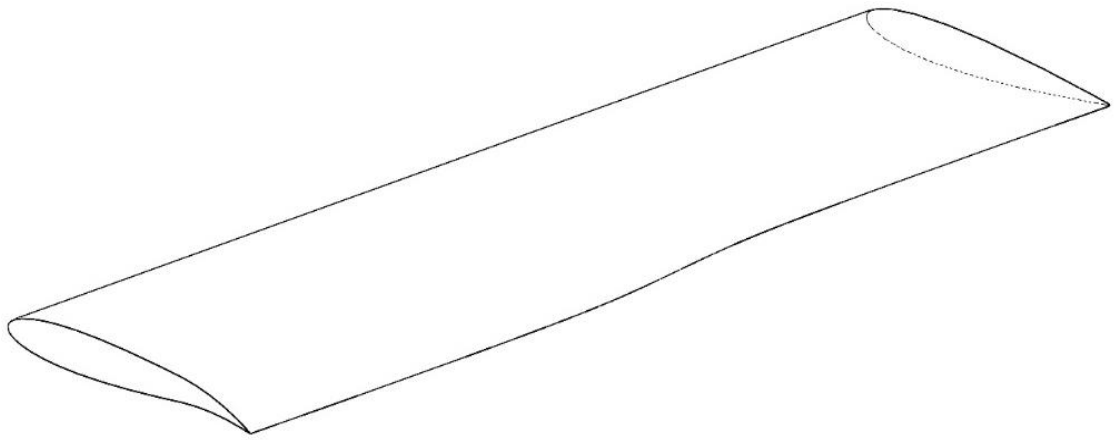

(b) Wing surface after the rib coordinates are passed to SolidWorks.

Figure 11. Wing model in MATLAB and SolidWorks.

Once all the geometries to be analyzed are created we can solve for the aerodynamic coefficients iteratively through a python script. A detailed explanation of python code is given in the following sections.

2.4.1. Design Modeler

In this part of the process, we do not use the python instead create the flow domain manually. Once we have the SolidWorks models for each wing geometry, the model is sent to ANSYS Design Modeler. Here we insert the fluid domain to the wing model and then subtract the wing body from the fluid domain. This gives use the fluid environment around the wing as our flow domain (see Figure 12).

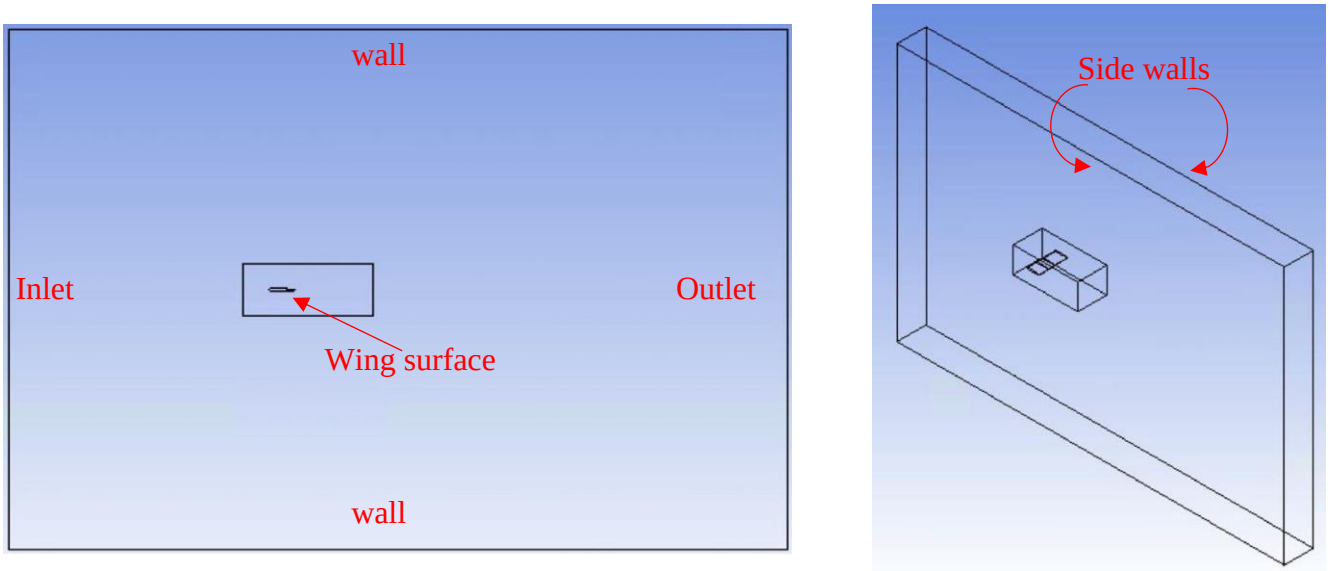

(a) Side View. (b) Iso-metric View.

Figure 12. Fluid domain.

The boundary conditions applied to the boundaries shown in Figure 12 are listed below:

- Inlet: Velocity inlet with velocity set to match the free stream velocity.
- Outlet: is set to be a pressure outlet.
- Walls and Wing surface: are the no-slip wall boundaries.

- Side walls: these boundaries are set to symmetry boundary conditions. This way we will not have interference from the side tip vortices.

2.4.2. Fluent meshing

Now that we have our flow domain, we are ready to mesh the domain and send it to the fluid dynamics solver. To mesh the domain, we start ANSYS Fluent through our python script in its meshing mode. The script writes a journal file which serves as a set of instructions that ANSYS Fluent follows. Although python writes one journal file which contains instructions for mesher and the solver, we will first discuss the meshing part and then the solver part in the subsequent section.

```
os.chdir("C:\\Users\\anarkhede\\Downloads\\transitionspan\\{0}".format(geom_name))

# write journal
journal = open("fluent_journal.jou",'w')
journal.write(r"sync-chdir C:\Users\anarkhede\Downloads\transitionspan\{0}".format(geom_name))
journal.write(r"""
(define study "Wing-CML")
(define factor 1)
""")
journal.write('(define fileName "{0}")'.format(geom_name))
journal.write(r"""
(ti-menu-load-string (format #f "file start-transcript ~a-~a-~02d.trn" fileName study factor))
(define global-min 1e-4)
(define global-max 0.2)
(define global-growth-rate 1.2)
(define local-growth-rate 1.2)
(define min-face-size-wing-le 1e-4)
(define max-face-size-wing-le 1e-3)
(define norm-angle-le 9)
(define min-face-size-wing-te 1e-4)
(define max-face-size-wing-te 1e-3)
(define norm-angle-te 2)
(define min-face-size-wing-mid 1e-3)
(define max-face-size-wing-mid 5e-3)
(define norm-angle-mid 18)
(define first-layer-height 1.25e-5)
(define number-of-layers 25)
(define boi-max 1e-2)
/beta-feature-access yes yes
file import cad-options save-PMDB? yes
(ti-menu-load-string (format #f "file import cad , ~a.agdb , , , m" fileName))
/size-functions set-global-controls global-min global-max global-growth-rate
/scoped-sizing create body-of-influence boi object-faces-and-edges yes no boi* boi-max global-growth-rate
/scoped-sizing create face-zones-wing-le curvature face-zone yes no wingsurfLE min-face-size-wing-le max-face-size-wing-le global-growth-rate norm-angle-le
/scoped-sizing create face-zones-wing-te curvature face-zone yes no wingsurfTE min-face-size-wing-te max-face-size-wing-te global-growth-rate norm-angle-te
/scoped-sizing create face-zones-wing-mid curvature face-zone yes no wingsurfMID min-face-size-wing-mid max-face-size-wing-mid global-growth-rate norm-angle-mid
/scoped-sizing compute
(ti-menu-load-string (format #f "file write-size-field ~a-~02d.sizing" fileName factor))
/file import cad-options save-PMDB? no
(ti-menu-load-string (format #f "file import cad-options tessellation cfd-surface-mesh yes ~a-~02d.sizing.sf" fileName factor))
(ti-menu-load-string (format #f "file import cad , ~a.agdb.pmdb , , , , m yes" fileName))
/objects volumetric-regions compute flowdomain no
/objects vol-reg change-type flowdomain (flowdomain) fluid
/mesh poly controls cell-sizing size-field
/mesh scoped-prisms create prism-wing uniform first-layer-height number-of-layers global-growth-rate flowdomain named-regions flowdomain selected-face-zones wing*
/mesh auto-mesh flowdomain yes scoped pyramids poly yes
/mesh modify auto-node-move (*) (*) 0.8 50 120 yes 10
(ti-menu-load-string (format #f "file write-mesh mesh-~a-~a.msh.gz" fileName study))
/mesh prepare-for-solve yes
/switch-to-solution-mode yes""")
journal.close()
```

Figure 13. Section of the python script that writes commands for building the mesh.

Figure 13 contains the part of the python script in which we write the instructions for meshing the domain. The journal file first creates a triangular surface mesh (see Figure 14) which is then grown gradually in the fluid domain to get the volume mesh (shown in Figure 15). We also

make use of the Body-of-Influence feature in Fluent meshing, which helps us to get a more refined mesh in the vicinity of the wing and a coarse mesh in the far field. This way we reduce the cell count but maintains the accuracy.

Also, the only difference between the viscous and inviscid mesh is that viscous mesh additionally has a boundary layer mesh containing 25 layers with a $y^+ \leq 1$.

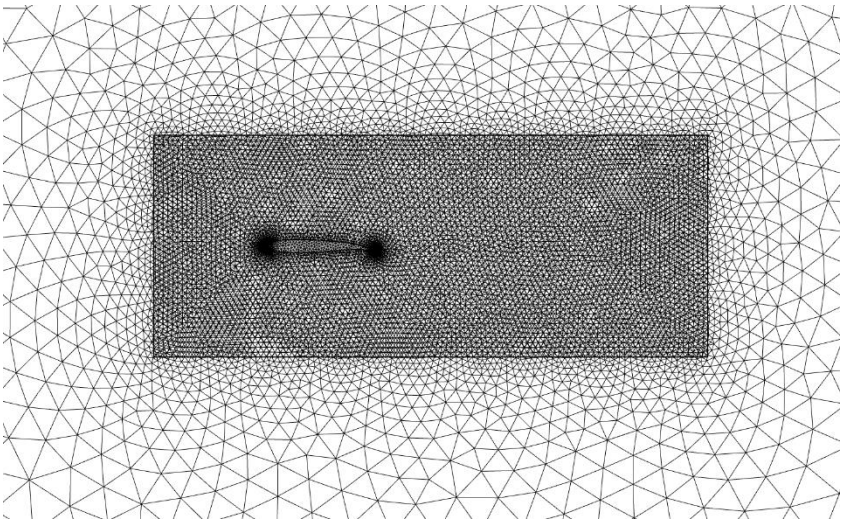

(a) Side view of the fluid domain surface mesh.

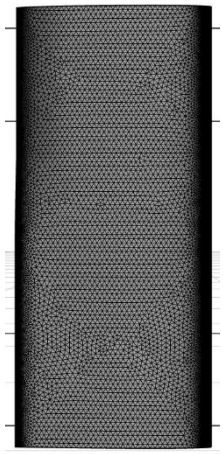

(b) Top view of the wing surface mesh

Figure 14. Surface mesh snapshots from ANSYS Fluent Meshing.

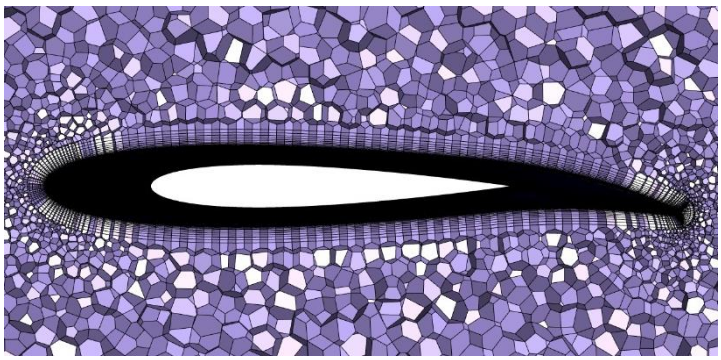

Figure 15. Volume mesh for viscous simulations.

The volume mesh for inviscid simulation is the same as the one for viscous study but, it lacks the boundary layers as they are not needed for inviscid flow solutions. Also, we have used ANSYS Fluent's in-built polygon mesher to mesh the fluid domain. The benefit of using polygon elements is that the computation time is very low. Additionally, a polygon mesh gives

almost the same results as a tetrahedral mesh but with lower cell count which saves memory and improves the computational time even further.

2.4.3. Fluent solver

The last step of our iterative process is to calculate the aerodynamic coefficients. This is done through a pressure-based viscous and inviscid solver. The viscous model adapted is the $k-\omega$ SST model discussed in Section 2.3. A short fragment of the python script that writes the journal file for Fluent in shown in Figure 16. This part of the journal file sets up Fluent solver and runs the steady state iterations. At the end of the iterations or when the solution is converged, the journal file saves the simulation and writes co-efficient of lift and drag to a data file which can be then imported to MATLAB for data visualization.

```
# write journal
journal.write("""
(define flowvel 20)
(define surf-area 0.09)
(define chord 0.2)
(define density 1.18625)
(define viscosity 1.825e-5)
(define pressure-op 100718.4519)
(define Tref 295.7844)
(define min-res 1e-4)
(define mom-relax 0.5)
(define press-relax 0.5)
(define Courant 50)
(define number-of-iteration 300)
/define models viscous kw-sst? yes
/define models viscous curvature-correction? yes
/define materials change-create air air yes constant density no no yes constant viscosity no no no
;/define boundary-conditions modify-zones zone-type flowdomain fluid
/define boundary-conditions modify-zones zone-type inlet velocity-inlet
/define boundary-conditions modify-zones zone-type farfield velocity-inlet
/define boundary-conditions modify-zones zone-type outlet pressure-outlet
;/define boundary-conditions wall shearwall no yes shear-bc-spec-shear no no 0 no 0.5 no 0 no 0 no 0
/define boundary-conditions velocity-inlet inlet yes yes no flowvel no 0 yes no 1 no 0 no 0 no no yes 5 10
/define boundary-conditions velocity-inlet farfield yes yes no flowvel no 0 yes no 1 no 0 no 0 no no yes 5 10
/define boundary-conditions pressure-outlet outlet yes no 0 no yes no no yes 5 10 no yes no no no
/define operating-conditions operating-pressure pressure-op
/solve set p-v-coupling 24
/solve set pseudo-transient no
/solve set warped-face-gradient-correction enable? no
/solve set discretization-scheme k 1
/solve set discretization-scheme omega 1
/solve set discretization-scheme pressure 12
/solve set discretization-scheme mom 1
/solve set p-v-controls Courant press-relax mom-relax
/report reference-values area surf-area
/report reference-values length chord
/report reference-values velocity flowvel
/report reference-values density density
/report reference-values viscosity viscosity
/report reference-values temperature Tref
/solve report-definitions add wing-drag drag force-vector 1 0 0 thread-names wingsurfte wingsurfle wingsurfmid () scaled? yes quit
/solve report-definitions add wing-lift lift force-vector 0 1 0 thread-names wingsurfte wingsurfle wingsurfmid () scaled? yes quit
;/solve report-plots add drag-plot report-defs (wing-drag) quit
;/solve report-plots add lift-plot report-defs (wing-lift) quit
/solve report-files add wing-drag-force frequency 1 report-defs (wing-drag) quit
/solve report-files add wing-lift-force frequency 1 report-defs (wing-lift) quit
/define parameters output-parameters create report-definition wing-drag quit
/define parameters output-parameters create report-definition wing-lift quit
(ti-menu-load-string (format #f "/solve report-files edit wing-drag-force file-name ~a~~a~~02d-drag.dat" fileName study factor))
(ti-menu-load-string (format #f "/solve report-files edit wing-lift-force file-name ~a~~a~~02d-lift.dat" fileName study factor))
/solve monitors residual check-convergence? yes yes yes yes no no quit
/solve monitors residual convergence-criteria min-res min-res min-res min-res quit
/solve initialize hyb-initialization
/file data-file-options pressure-coefficient velocity-magnitude y-plus quit
/file read-macro benchmark.scm
(benchmark '(iterate number-of-iteration))
/report fluxes mass-flow yes no
(ti-menu-load-string (format #f "report forces wall-forces no wingsurfte wingsurfle wingsurfmid () 1 0 0 yes ~a~~a~~02d-drag-force-report.dat" fileName study factor))
(ti-menu-load-string (format #f "report forces wall-forces no wingsurfte wingsurfle wingsurfmid () 0 1 0 yes ~a~~a~~02d-lift-force-report.dat" fileName study factor))
(ti-menu-load-string (format #f "report summary yes ~a~~a~~02d-fluent-summary.dat" fileName study factor))
(ti-menu-load-string (format #f "file write-case-data ~a~~a~~02d-solved.cas.gz" fileName study factor))
/file stop-transcript
exit""")
journal.close()
```

Figure 16. Section of the python script that writes commands for Fluent solver.

3. Results

Before we discuss the effects of changing the shape and size of the transition zone, we need to verify that the models developed – both viscous and inviscid – are valid representations of the flow field around the wing. Hence, in the subsequent sections we will first verify that the models developed give reliable information regarding the fluid flow around the wing. Then, we will discuss the effects of changing the shape and size of the transition region on the aerodynamic quantities like coefficients of lift and drag, and aerodynamic efficiency.

3.1. Verification

The verification process will be conducted in two steps. First, we will test both models with standard NACA 0012 rectangular wing. As this study is using symmetry boundary conditions on the side walls, the flow around the NACA 0012 rectangular wing will be essentially two dimensional, and thus will not have any spanwise variation. Aerodynamic quantities for this wing are widely available in the literature and it is easy to incorporate in our current computation model. Finally, we will compare the aerodynamic quantities of our wing model (with linear transition region) with the results published by [11].

3.1.1. NACA 0012 rectangular wing

A NACA 0012 rectangular wing model with $chord = 0.2\,m\ and\ span = 0.45\,m$ was developed in SolidWorks This model was then tested using the procedure outlined in Section 2.4. The experimental (viscous) results were obtained from [16] and a comparison between the coefficient of lift retrieved from our model and the values given in [16] is shown in the following figure.

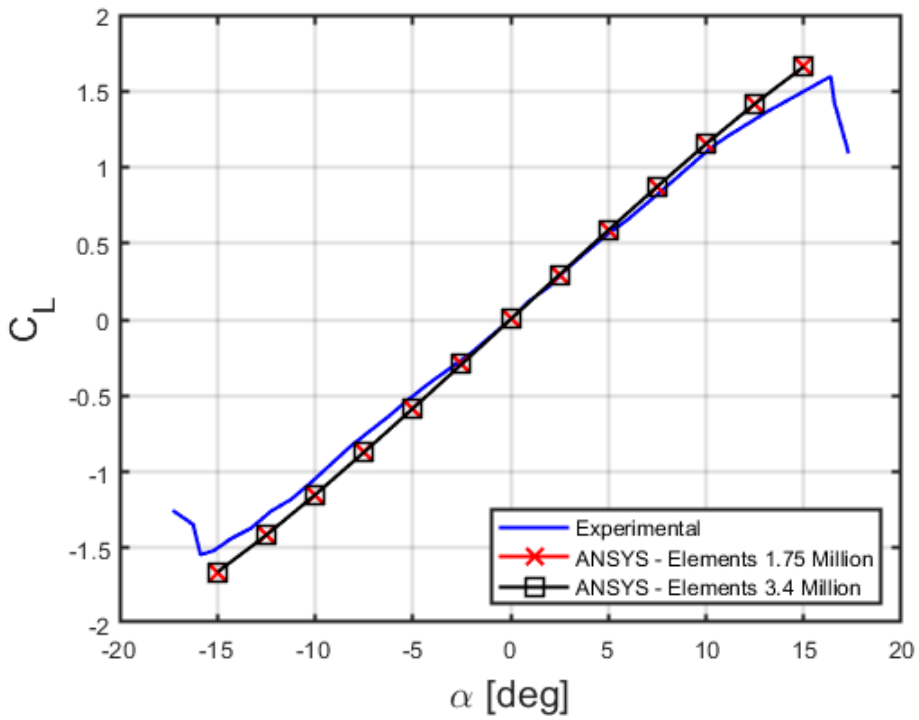

Figure 17. Coefficient of lift vs angle of attack for NACA 0012 wing without viscous effects.

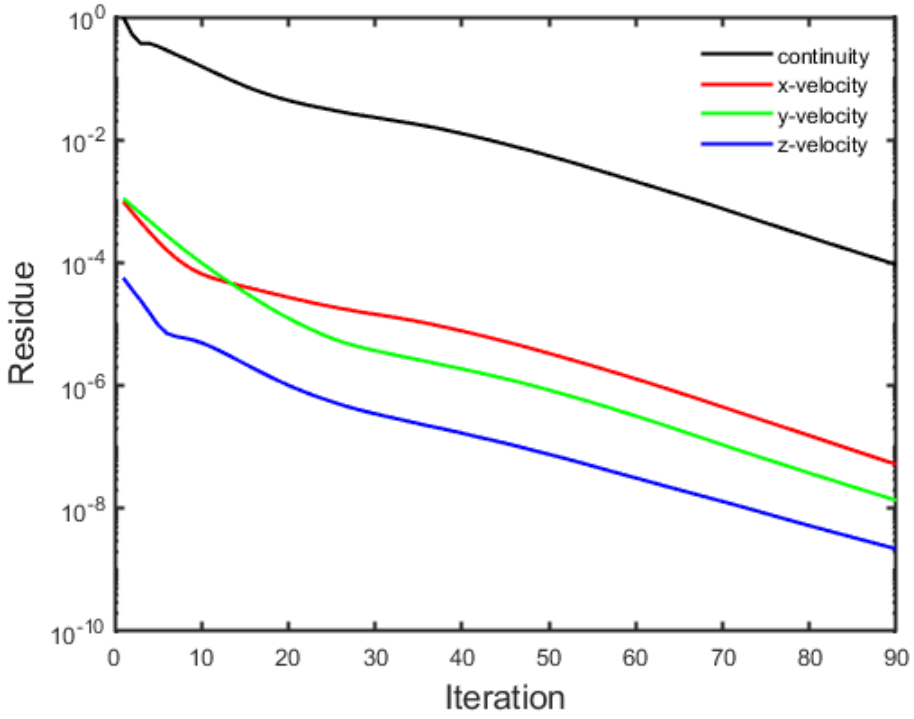

(a) Residue

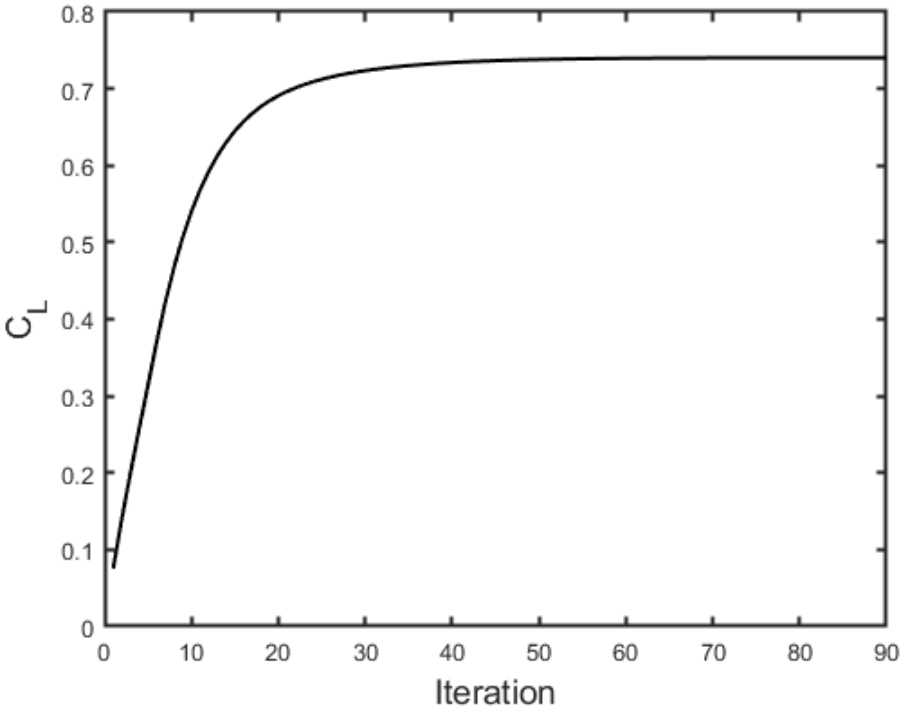

(b) Coefficient of lift

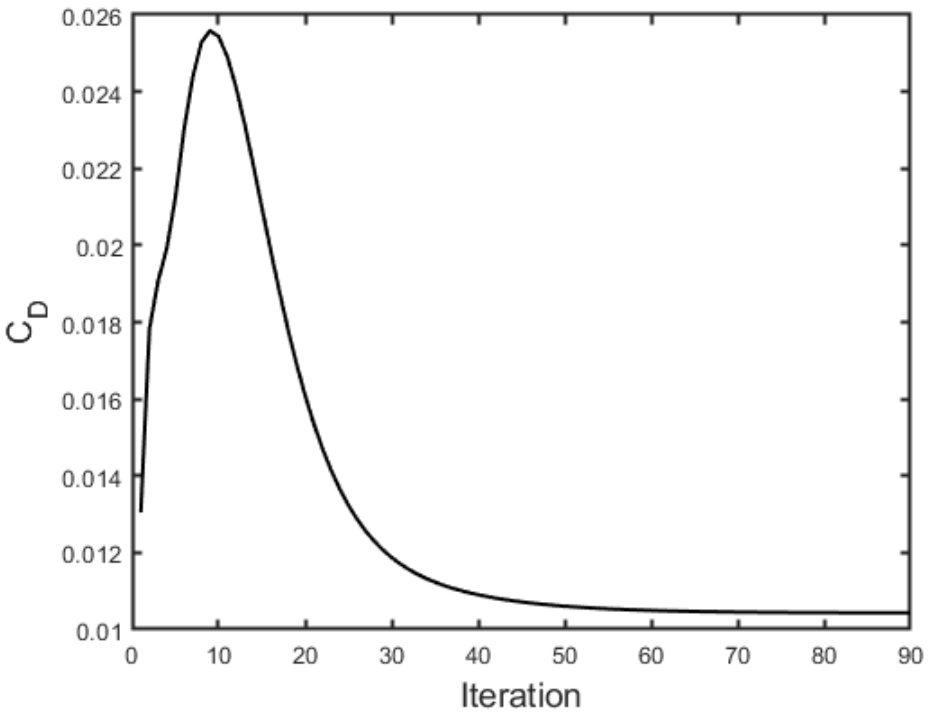

(c) Coefficient of drag

Figure 18. Iteration history of Inviscid simulation for NACA 0012 at an angle of attack of 10°.

The plot shows that the results obtained using the computational model described in Section 2.2 are in good agreement with the experimental data available in [16]. The model only diverges near stall conditions. Due to separation of flow from the wings surface near stall conditions, a loss in lift is observed. However, inviscid solver cannot capture this separation due to an absence of viscosity in the mathematical model and hence we see that Inviscid ANSYS lift coefficients continue to increase in Figure 17. Another observation is that the solution is mesh independent as the lift polar for the two meshes shown in Figure 17 are coincident.

In Figure 18(a) we observe that both conservation of mass and conservation of momentum equations have a residue below the required convergence criteria of 10−4. Furthermore, coefficient of lift and drag (which are the desired output of the solution process) have reached

a steady value. Thus, from Figure 17 and Figure 18 we can say that the model developed is both mesh independent and has a converged solution.

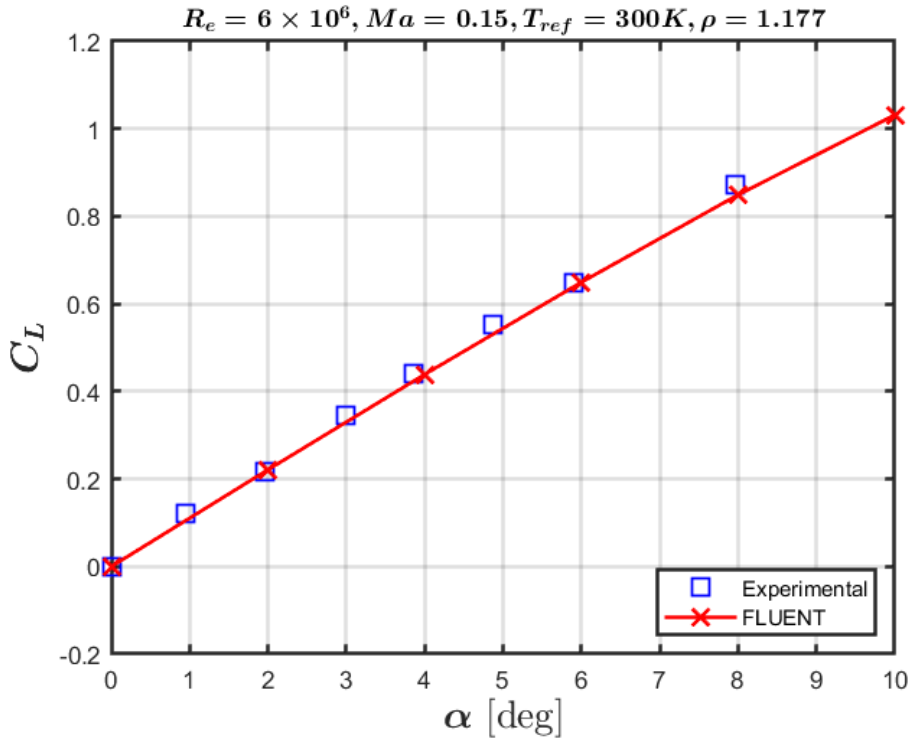

Figure 19. Coefficient of lift vs angle of attack for NACA 0012 wing with viscous effects.

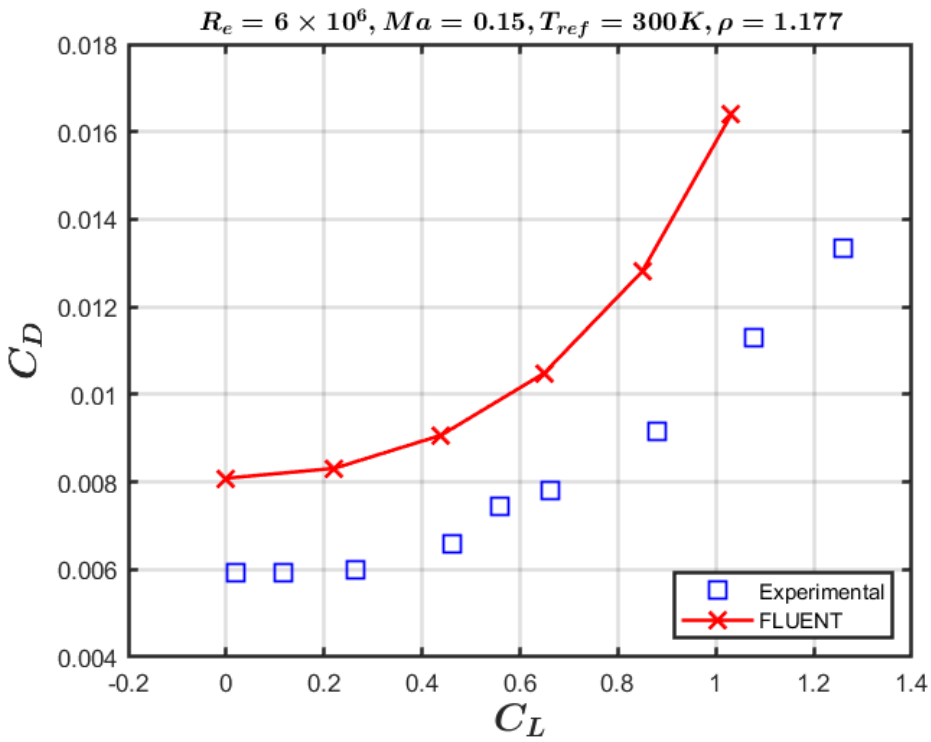

Figure 20. Coefficient of drag vs angle of attack for NACA 0012 wing with viscous effects.

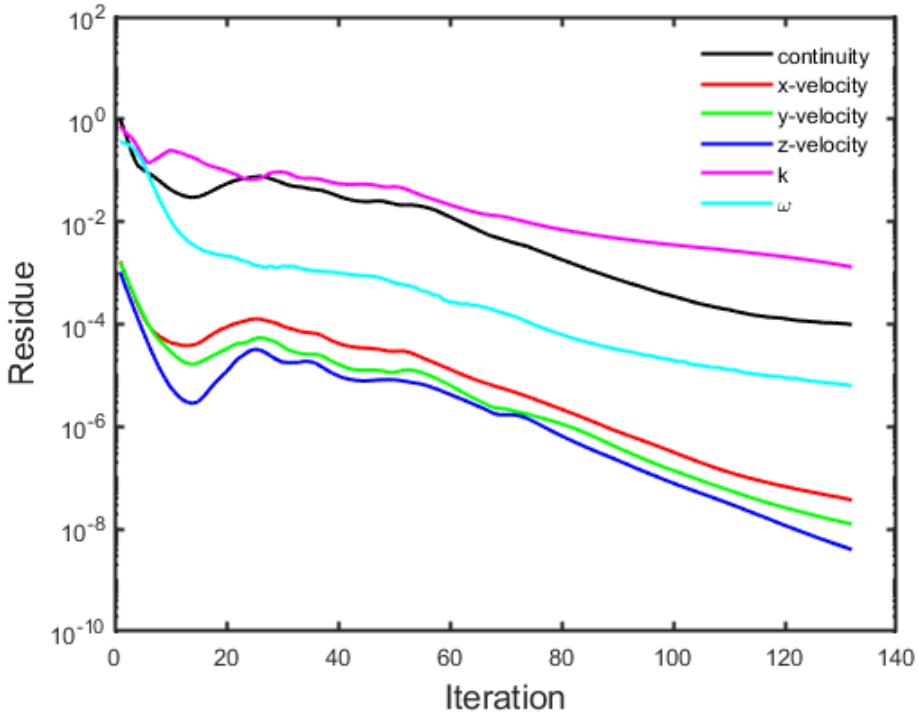

(a) Residue

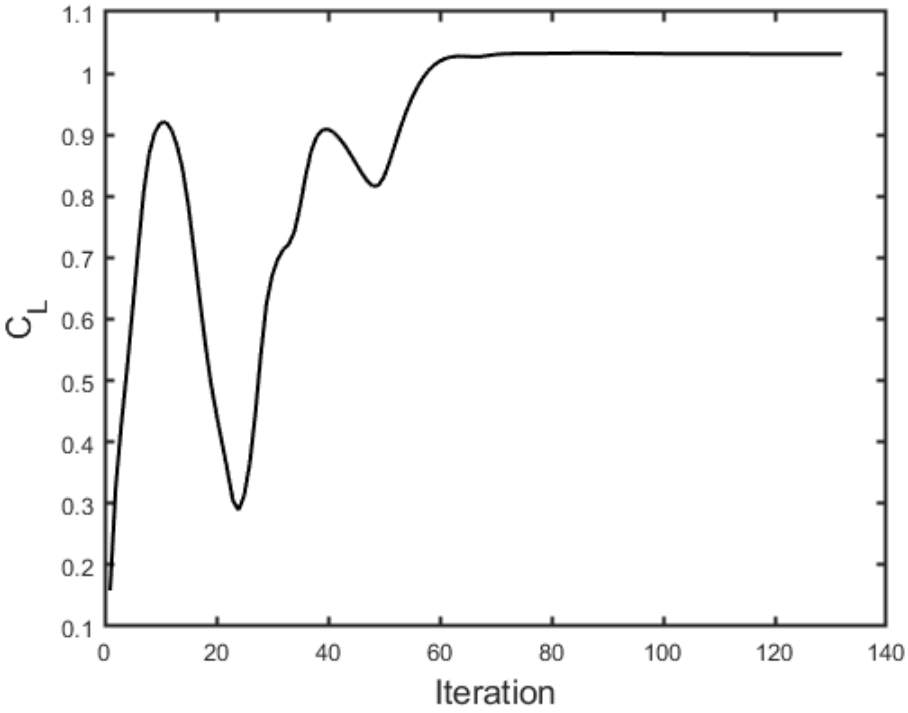

(b) Coefficient of lift

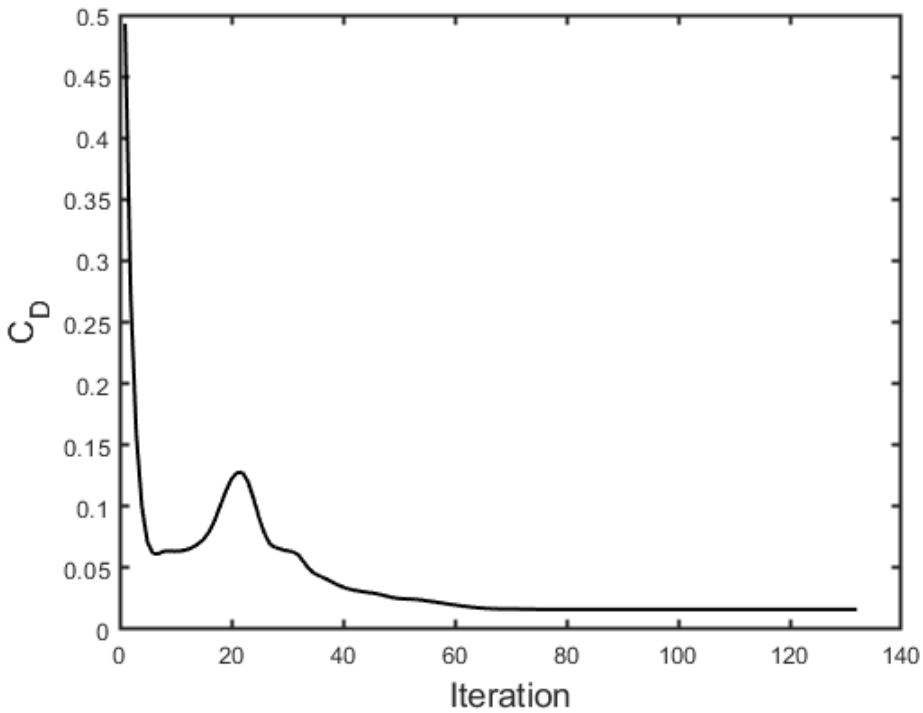

(c) Coefficient of drag

Figure 21. Iteration history for viscous $k - \omega$ SST simulation of NACA 0012 at an angle of attack of 10°.

As for the viscous data, we again see that the coefficient of lift (shown in Figure 19) is in good correlation with the experimental results given in [16], with an average relative error of 2.76%. However, this is not the case for coefficient of drag (see Figure 20). There might be various reasons for the error in coefficient of drag such as surface roughness not modeled correctly, dynamic viscosity and turbulence intensity not the same as experiments. It is usually difficult to exactly match the drag values obtained from a computational study and experiment without having the complete knowledge about the flow conditions and experiment environment.

The viscous model also produces a converged solution as observed in Figure 21. The primary outputs – lift and drag – have also attained a steady value. Hence, we can say with confidence that increasing the number of iterations won't affect the coefficients of lift and drag and hence would only add to the computational cost.

3.1.2. Wing with linear transition region

The previous section established that the models developed provide reliable information regarding the forces generated by a standard rectangular wing without flaps. In this section we will use the flapped wing geometry mentioned in [11] and calculate their aerodynamic coefficients using our viscous model. Their study comprised of two flap configurations: one being flap at a fixed flap deflection and the in the other configuration flap deflection was changed periodically. In both configurations the transition zone was linear shaped (see Figure 22). We will be focusing on their study related to the static flap configuration. The wing was tested for $Re = 0.62 \times 10^6$ and $Ma = 0.115$ and the aerodynamic quantities were calculated using a viscous $k - \omega$ SST CFD model. A comparison study with their model will verify whether our model works for flapped configurations or not.

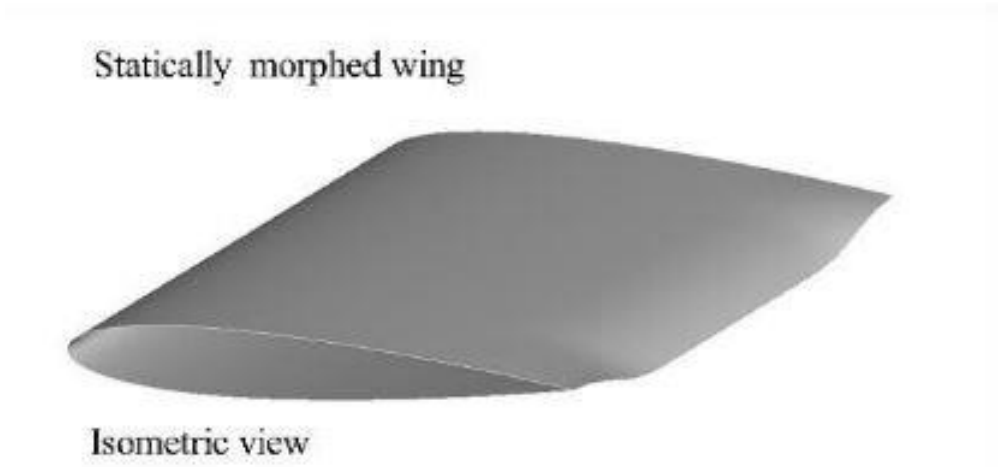

Figure 22. Isometric view of statically morphed wing used in [11].

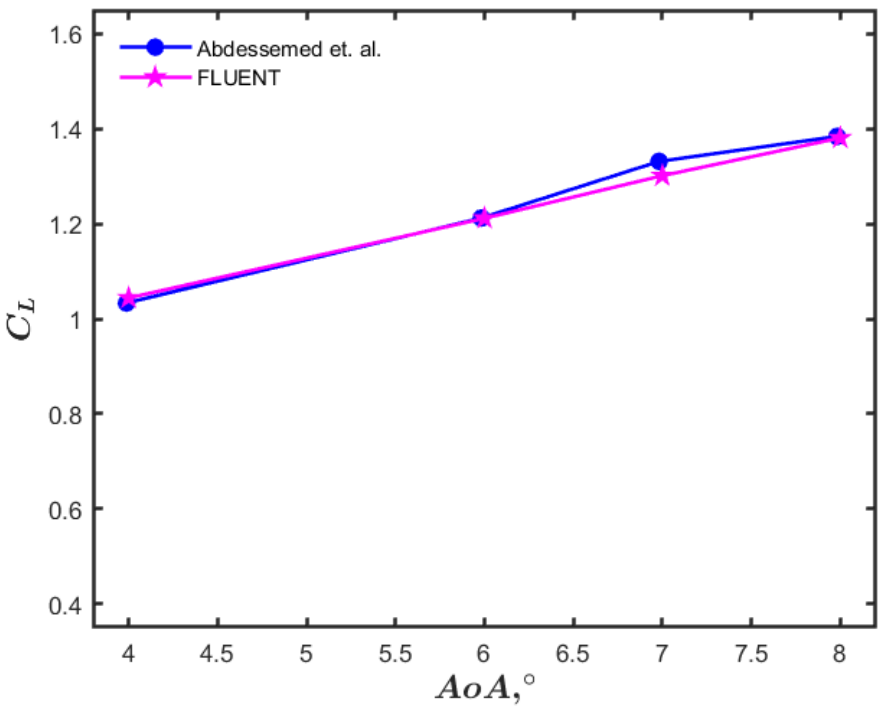

Figure 23. Coefficient of lift vs angle of attack for the wing geometry specified in [11].

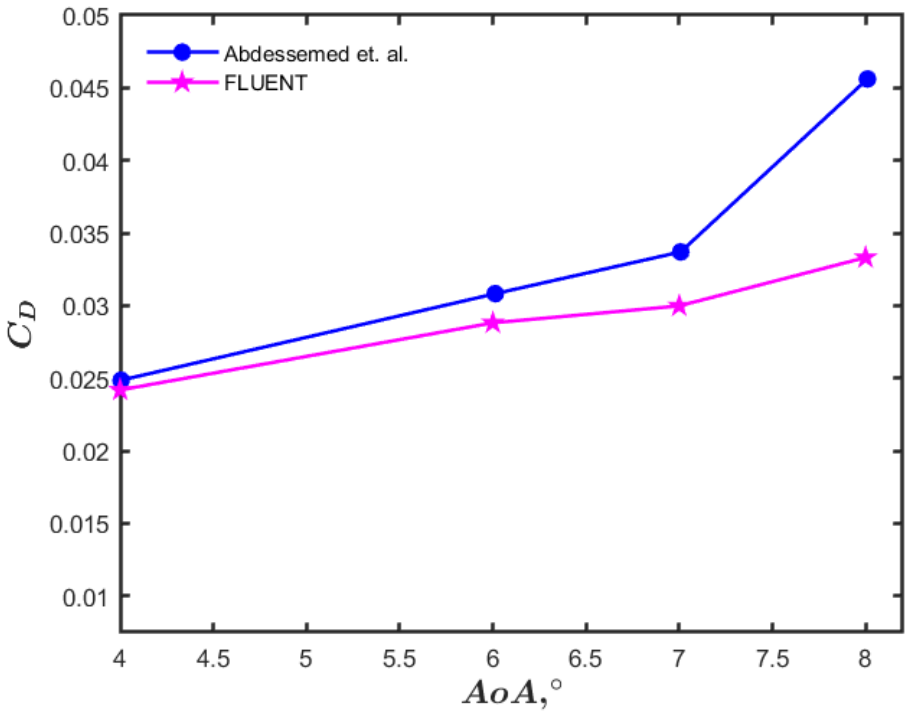

Figure 24. Coefficient of drag vs angle of attack for the wing geometry specified in [11].

Figure 23 and Figure 24 show that our viscous gives results that are in good correlation with those published in [11] for small angles of attack. However, it is important to note that in Figure 24, the largest difference in the coefficient of drag is at an angle of attack of 8°. This is due to the influence of unsteady flow dynamics in the model. From the convergence plot shown in Figure 25, it is evident that the flow field is highly unsteady and evaluating it with a steady state solver would give solutions that is iteration dependent, as the solution will not converge. Since in our study we will be focusing on low angles of attack, a steady state pressure-based viscous model seems to be sufficient.

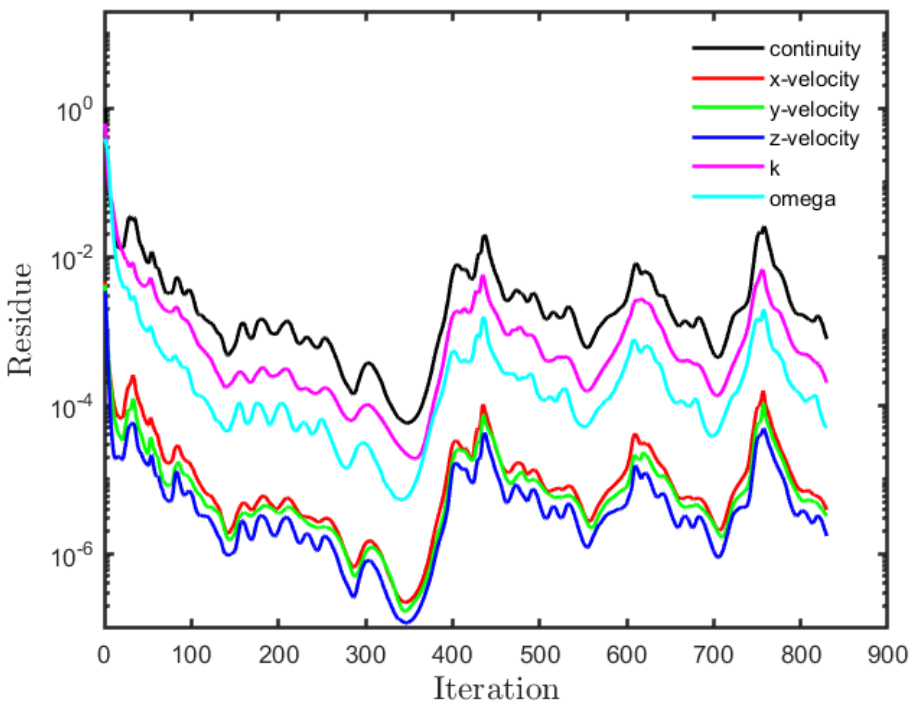

Figure 25. Residue convergence plot for the wing specified in [11] placed at an angle of 8^0.

From the discussion above we have established that are model gives reliable information regarding the flow field and the aerodynamic coefficients.

3.2. Effect of span and slope of the transition zone

In the following sections we will use the model described in the previous sections to understand the effects of span and slope of the transition zone on the wing's aerodynamic performance.

For all the studies the wing geometry and flow conditions used are:

$Geometry$:	$b\ (half - span) = 0.45m$
	$c\ (chord) = 0.2m$
	$c_f (flap\ chord) = 0.06m$
	$\delta_f (flap\ deflection) = 8^o$
$Flow\ Conditions$:	$Re_c = 2.6 \times 10^5$
	$U_\infty = 20\, m/s$
	$Ma = 0.058$

3.2.1. Effect of Slope

Inviscid studies were undertaken first as it is quite difficult to directly jump into viscous simulations without knowing a few esoteric mesh details that are required. Inviscid simulation does not require very intricate mesh details (like boundary layers, y+ etc.), it is easy to setup its boundary conditions, and its convergence is faster. This means that it provides a computationally cheap proof of concept.

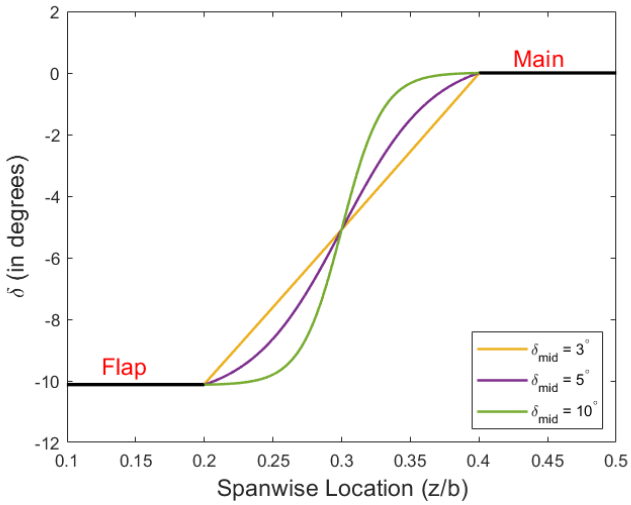

Figure 26. Trailing edge profile of a continuous mold-line link flap with the seamless transition parametrized by a hyperbolic tangent curve.

The following figures show the dependence of performance parameters – like coefficient of lift, drag and aerodynamic performance – on the slope of the transition zone at mid-point (see Figure 26 for reference). In each figure the initial point always corresponds to a linear transition zone.

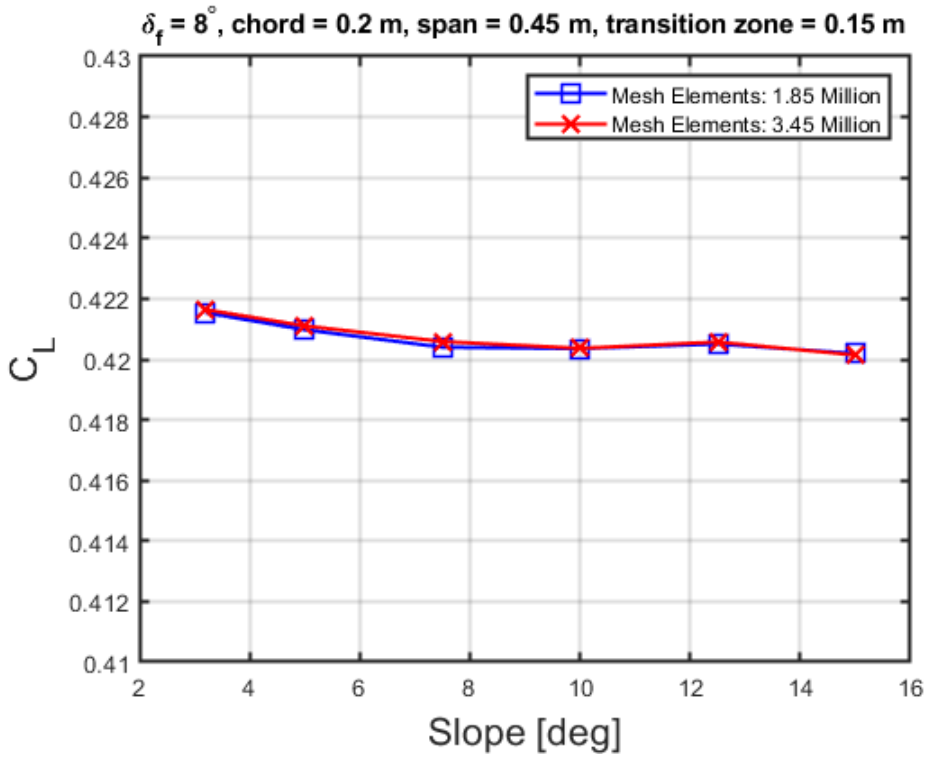

Figure 27. Variation of coefficient of lift (C_L) with slope of the transition zone at mid-point for an angle of attack of $\alpha = 0^o$ in inviscid flow conditions.

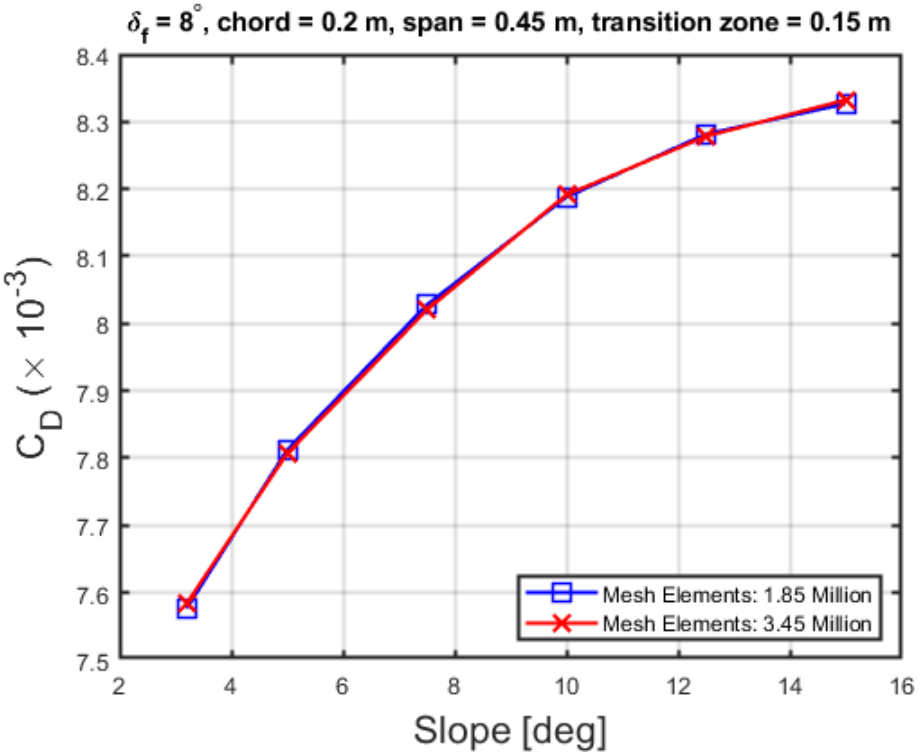

Figure 28. Variation of coefficient of drag (C_D) with slope of the transition zone at mid-point for an angle of attack of $\alpha = 0^o$ in inviscid flow conditions.

Figure 27 shows that the coefficient of lift remains almost constant as the slope of the transition zone is increased. From the plot it looks like the value of lift stays relatively constant with increase in slope.

In Figure 26 increasing the slope means that the curvature near flap and main airfoil increases. The curvature at these two locations however is exactly opposite to one another. That is if flap has a curvature that is concave upwards then the curvature near the main airfoil is concave downwards. This opposing curvature means that these two regions tend to balance out their effects and hence we see an almost constant lift coefficient. Similar effect is seen for coefficient of drag – Figure 28. Here however, the aerodynamic effect of the flap curvature outweighs the aerodynamic effect of the curvature near the main airfoil, which is why there is a noticeable amount of change in drag coefficient.

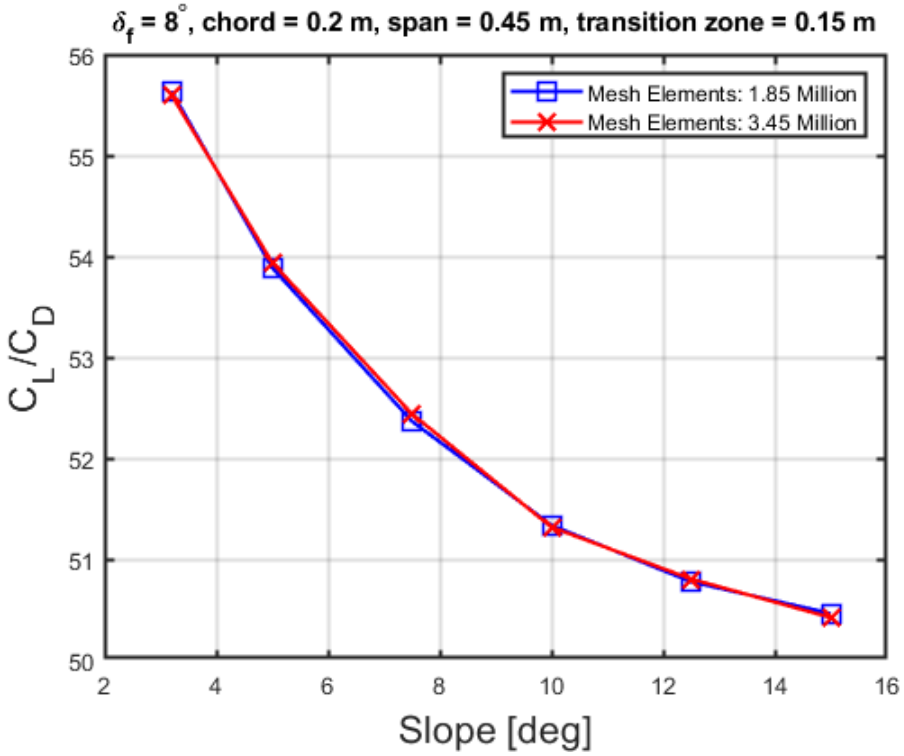

Figure 29. Variation of aerodynamic performance (C_L/C_D) with slope of the transition zone at mid-point for an angle of attack of $\alpha = 0^o$ in inviscid flow conditions.

Due to the noticeable change in drag and almost constant lift, the aerodynamic performance of the linear slope is much better in comparison to the transition zone with hyperbolic tangent curvature – as found in Figure 29. This is in line with the results published in Kamliya Jawahar, Zang and Azarpeyvand [8].

3.2.2. Effect of Span

In this section we will look at the aerodynamic effects of transition zone span (s). To keep the slope uniform between different span cases, we have chosen to maintain the slope equal to linear transition zone. So, for each span test case, the shape of the transition zone would be a straight line.

3.2.2.1. Inviscid flow

The following three figures show the variation of coefficient of lift (C_L), coefficient of drag (C_D) and aerodynamic performance (C_L/C_D) for different angles of attack with inviscid flow conditions.

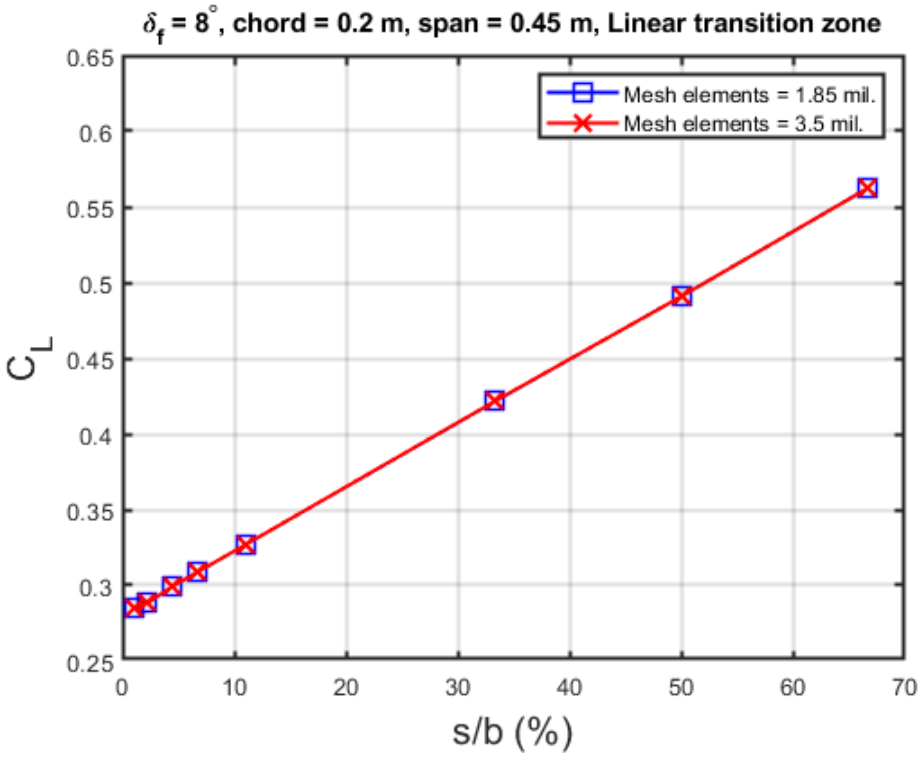

(a) $\alpha = 0^0$

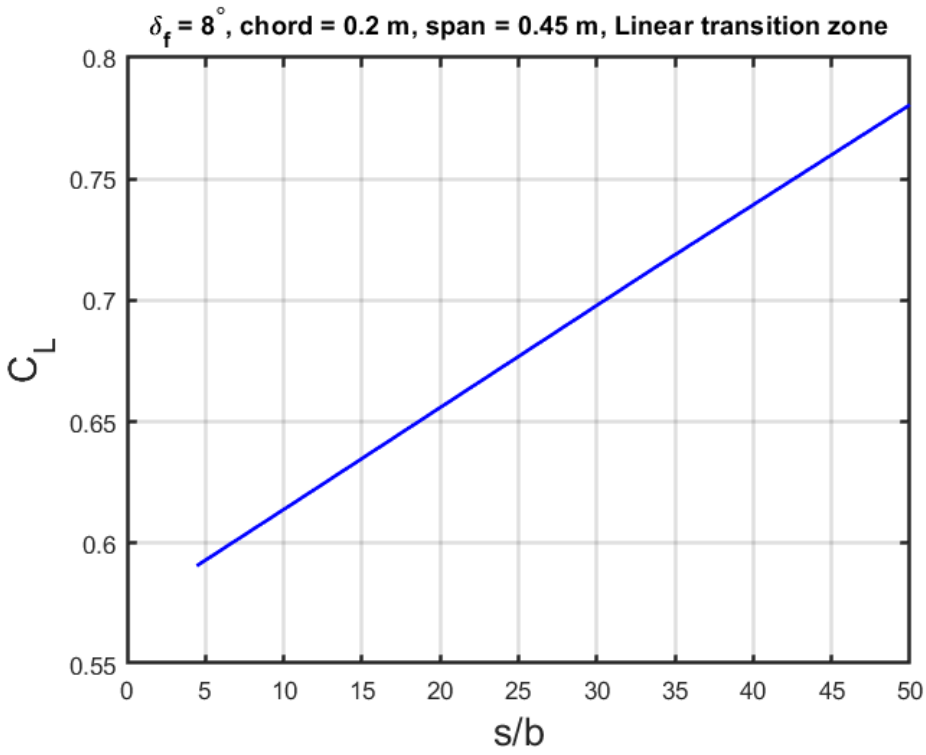

(b) $\alpha = 2.5^0$

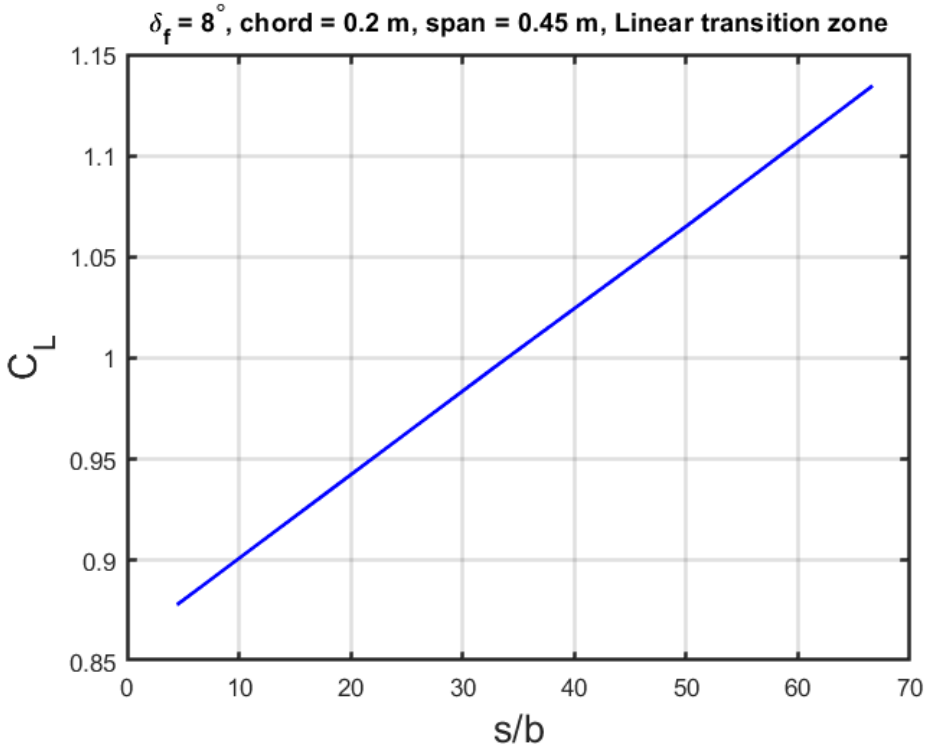

(c) $\alpha = 5^0$

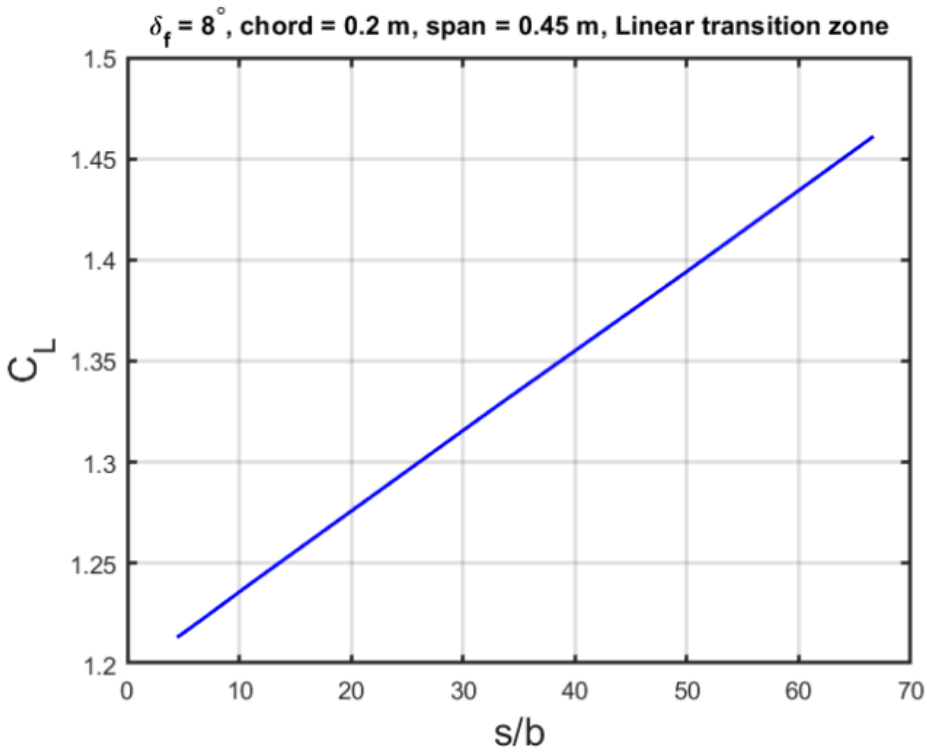

(d) $\alpha = 8^0$

Figure 30. Variation of coefficient of lift (C_L) with transition zone span (s) to wing half span (b) ratio for different angles of attack (α) in inviscid flow conditions.

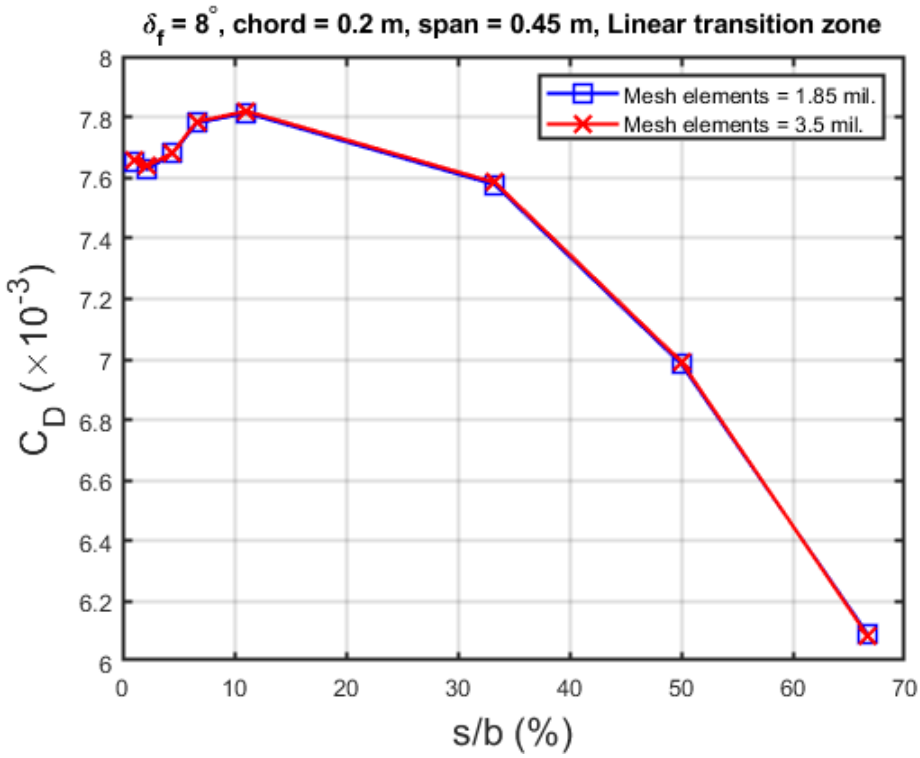

(a) $\alpha = 0^0$

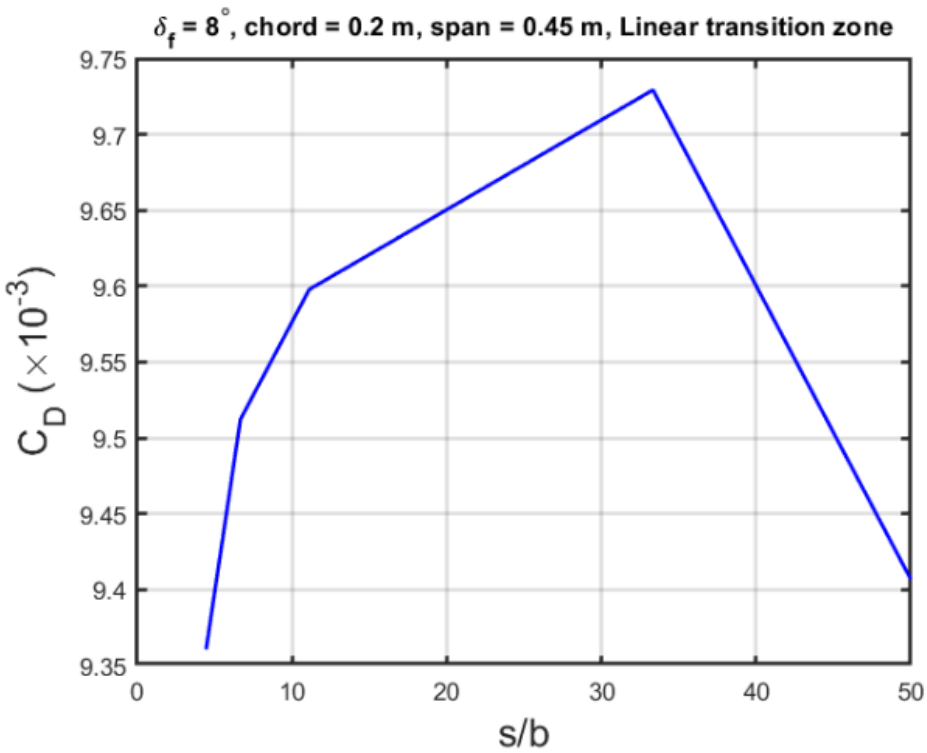

(b) $\alpha = 2.5^0$

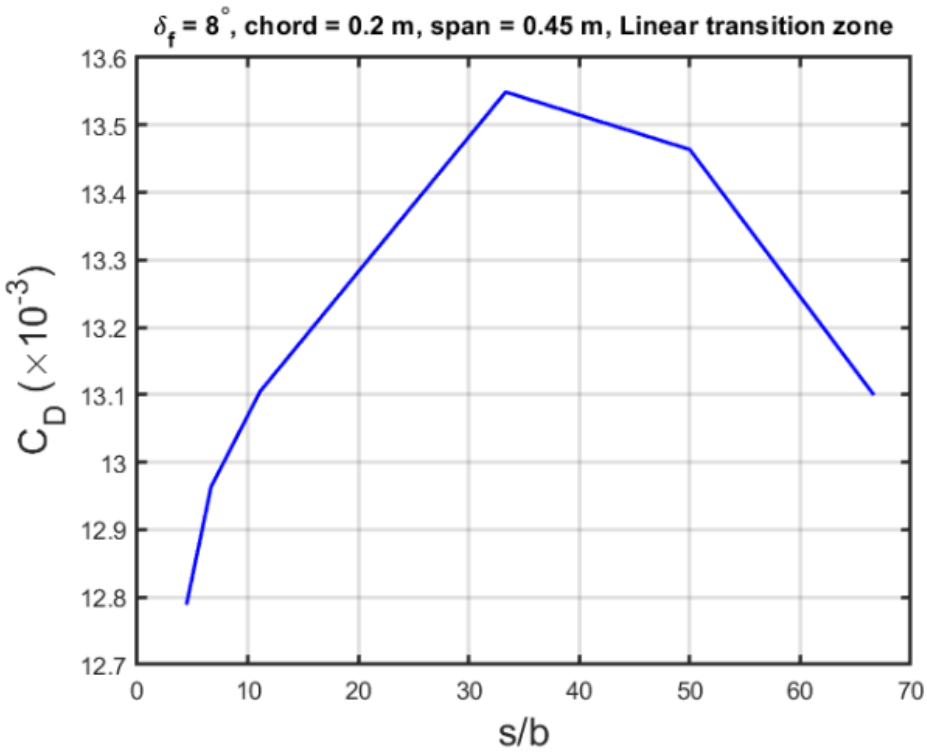

(c) $\alpha = 5^0$

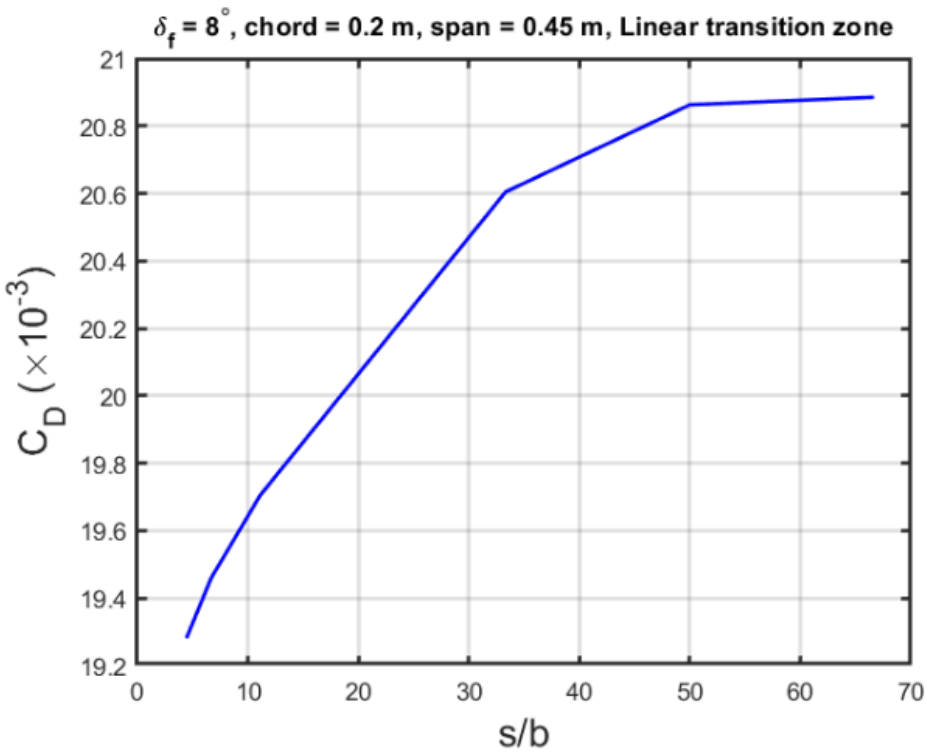

(d) $\alpha = 8^0$

Figure 31. Variation of coefficient of drag (C_D) with transition zone span (s) to wing half span (b) ratio for different angles of attack (α) in inviscid flow conditions.

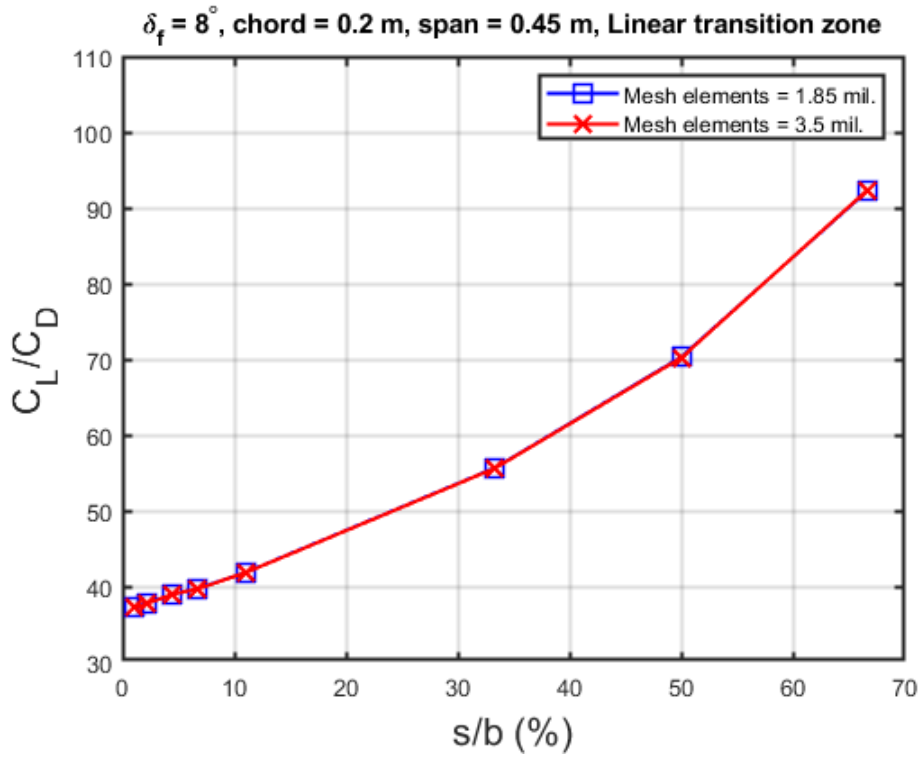

(a) $\alpha = 0^0$

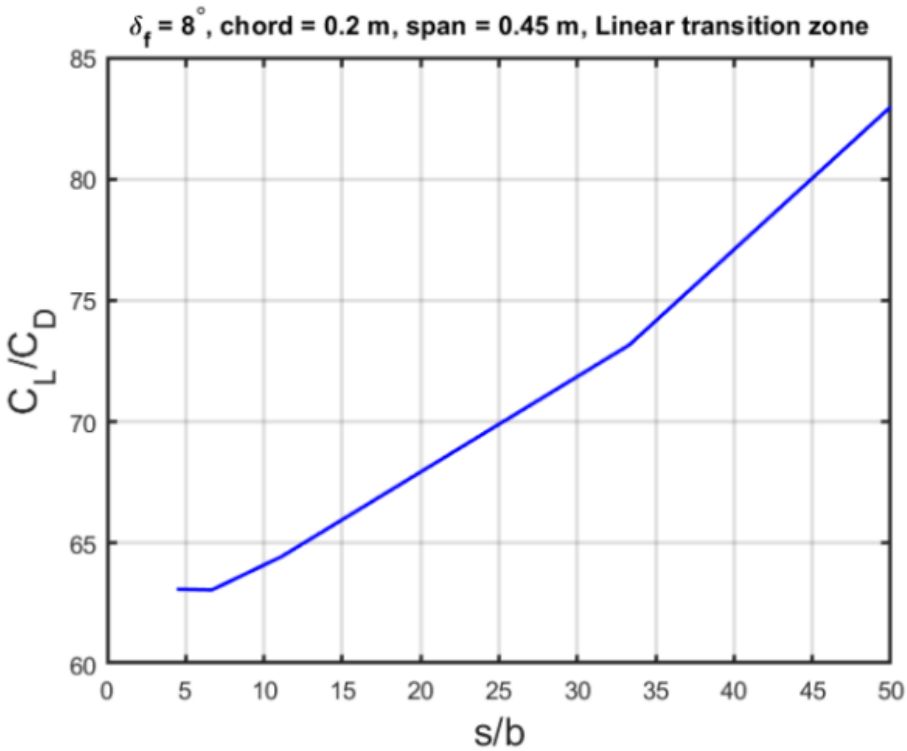

(b) $\alpha = 2.5^0$

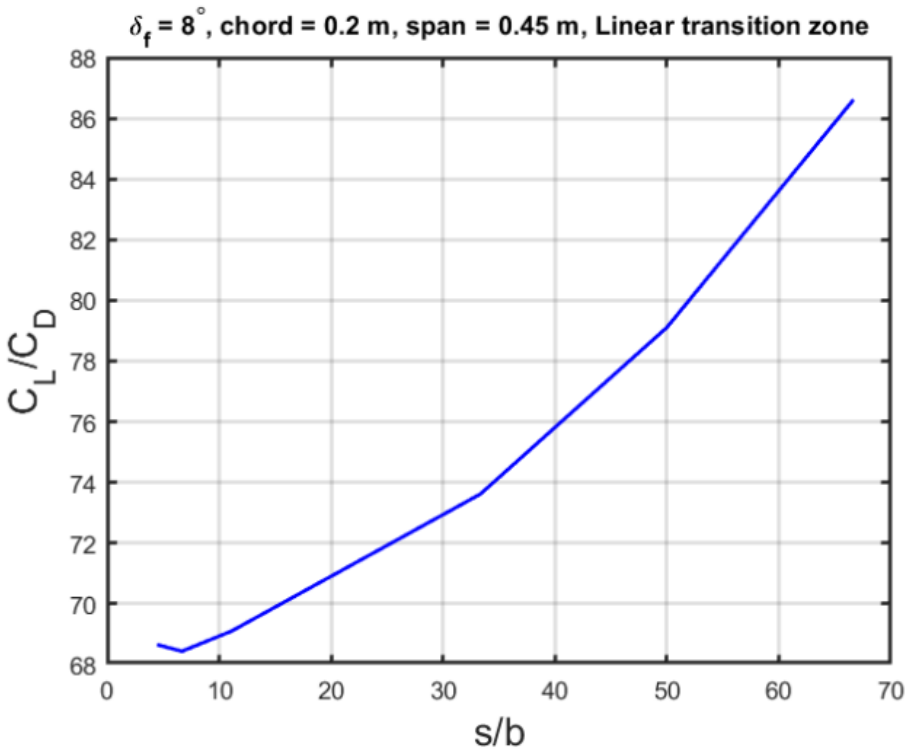

(c) $\alpha = 5^0$

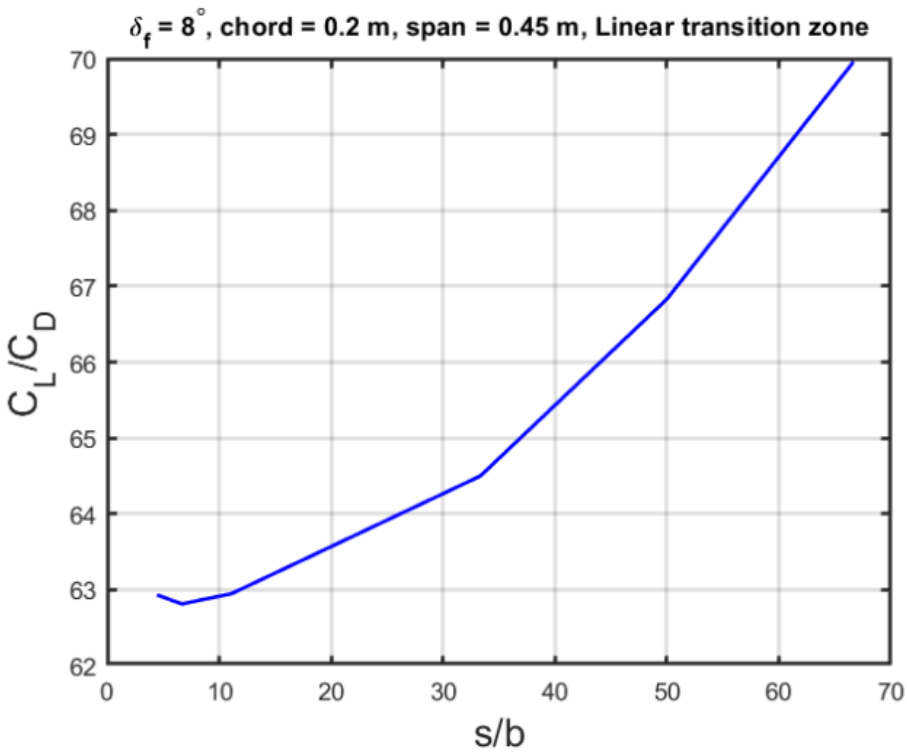

(d) $\alpha = 8^0$

Figure 32. Variation of aerodynamic performance (C_L/C_D) with transition zone span (s) to wing half span (b) ratio for different angles of attack (α) in inviscid flow conditions.

From Figure 30, it is found that increasing the span of the linear transition zone increases the amount of lift. This is expected because when we increase the span of the transition zone, the airfoil sections which were initially at no flap deflection would be now at a finite flap angle. Due to the increase in flap deflection more fluid is being pushed downwards and hence the increase in lift. This would also mean that more fluid is being obstructed by the transition zone and would lead to increase in drag too – as seen for the first few transition zone spans in Figure 31. However, the interesting result to note in Figure 31 is that although initially drag increases as we increase the transition zone span, after a certain span it starts to go down. The peaks in Figure 31 show that there is clearly an optimum transition zone span which would produce the maximum drag at a certain angle of attack. Also, as we increase the angle of attack this peak tends to slowly shift to the right. Because of the decrease in drag (see Figure 31) and continuous increase in lift (see Figure 30), in Figure 32 we see an exponential increase in aerodynamic efficiency.

3.2.2.2. Viscous flow

Once we were accustomed to ANSYS Fluent, we also ran viscous simulations. The viscous study was conducted using the $k-\omega$ SST model – described in section 2.3. The results obtained from these simulations are listed below.

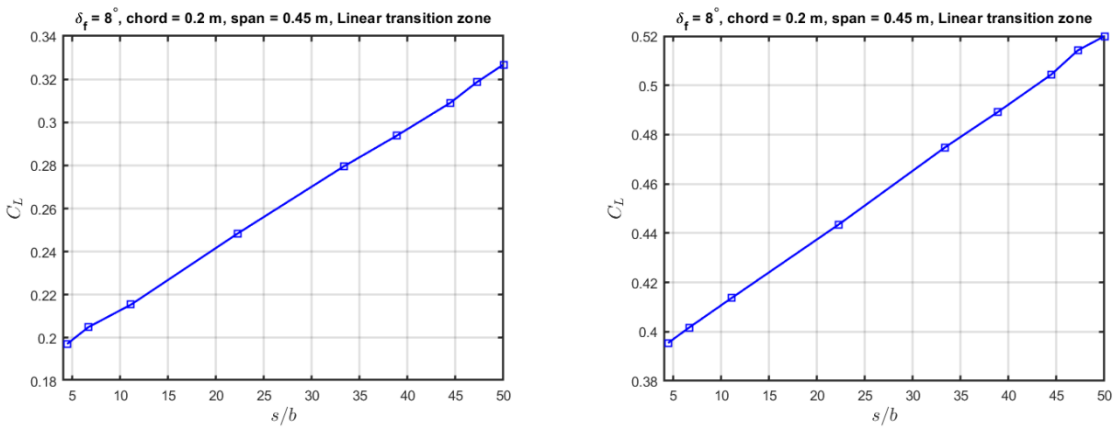

(a) $\alpha = 0^0$ (b) $\alpha = 2^0$

Figure 33. Variation of coefficient of lift (C_L) with transition zone span (s) to wing half span (b) ratio for different angles of attack (α) in viscous flow conditions.

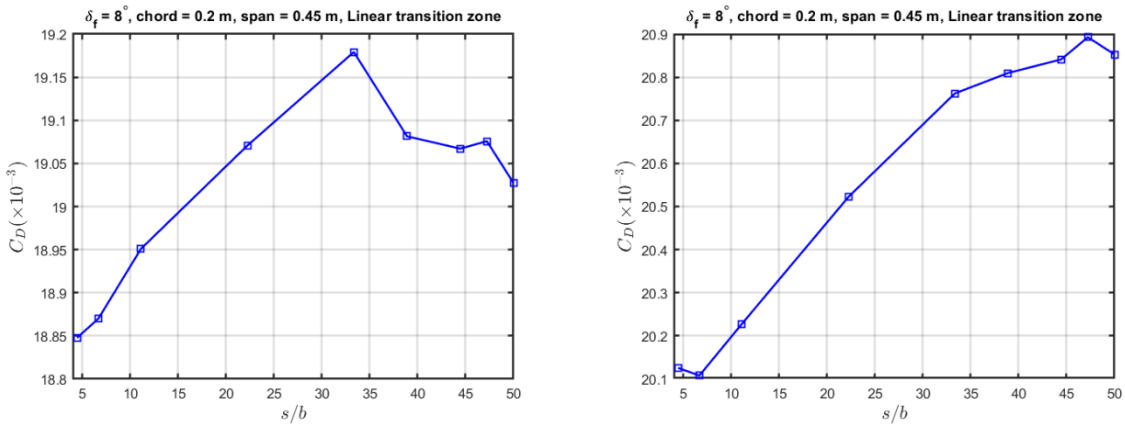

(a) $\alpha = 0^0$ (b) $\alpha = 2^0$

Figure 34. Variation of coefficient of drag (C_D) with transition zone span (s) to wing half span (b) ratio for different angles of attack (α) in viscous flow conditions.

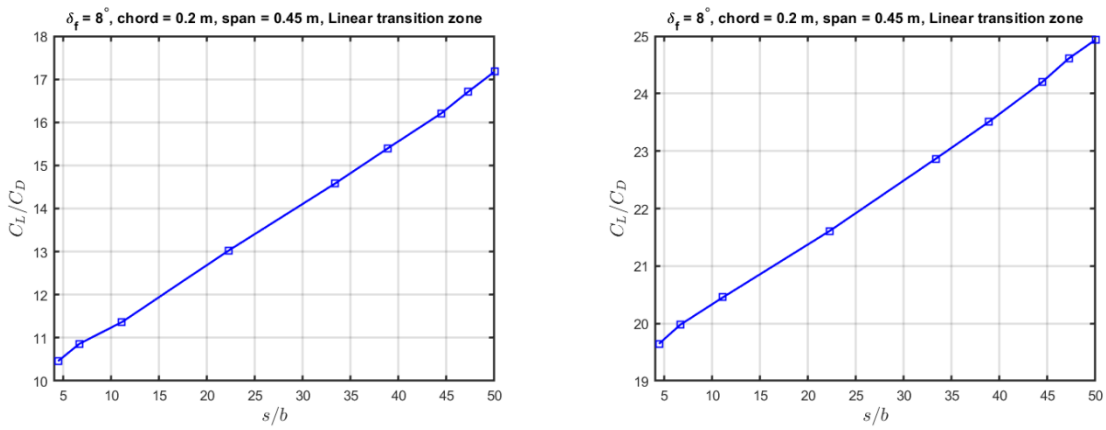

(a) $\alpha = 0^0$ (b) $\alpha = 2^0$

Figure 35. Variation of aerodynamic performance (C_L/C_D) with transition zone span (s) to wing half span (b) ratio for different angles of attack (α) in viscous flow conditions.

In Figure 33, we found that the trends are similar to inviscid simulations that being increase in coefficient of lift with increase in transition zone span the reason being the same as that stated for inviscid results. We again found that there is a clear peak where the coefficient of drag is maximum (see Figure 34) and that the peak shifts to the right as the angle of attack is increased. However, for viscous simulations this shift is much faster. This could be attributed to the dominant grad term, viscous drag. As the angle of attack is increased, viscous drag increases at a much faster rate compared to pressure drag which causes the peak to shift at a faster pace.

3.2.2.3. CML vs Conventional flaps

The main objective of this study was to see how these continuous mold-line link flaps (see Figure 11) fare against conventional flaps (see Figure 8).

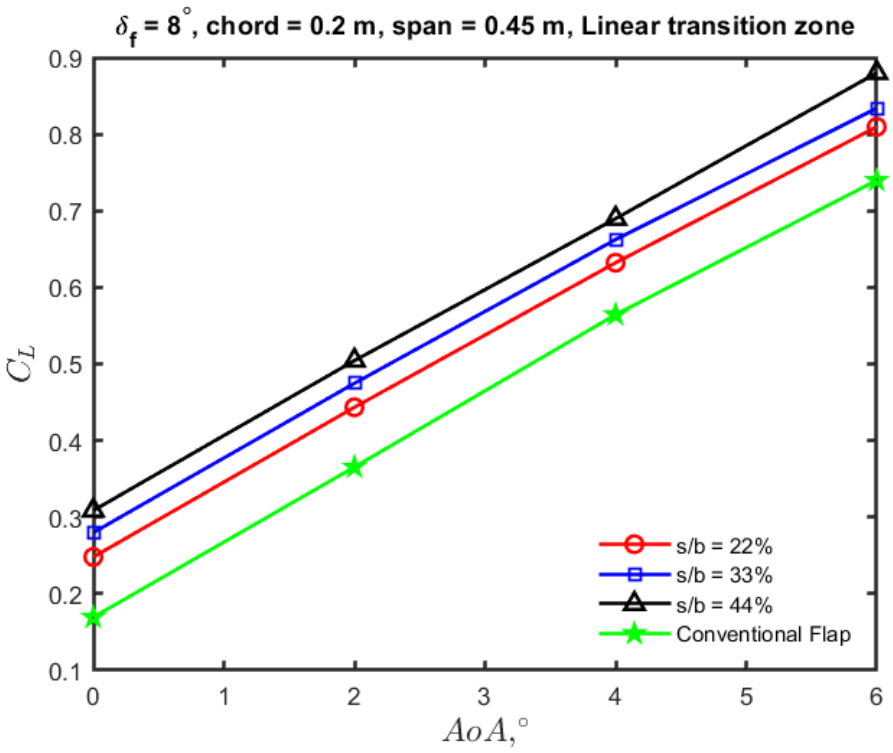

Figure 36. Coefficient of lift (C_L) comparison between conventional hinged parabolic flap and continuous mold-line link flap for viscous flow conditions.

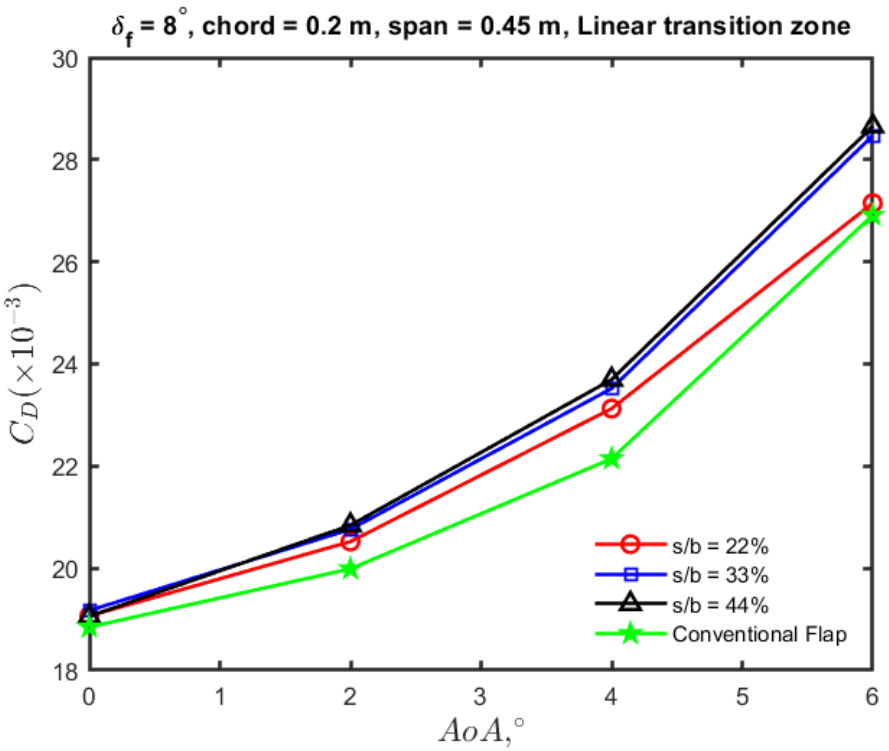

Figure 37. Coefficient of drag (C_D) comparison between conventional hinged parabolic flap and continuous mold-line link flap for viscous flow conditions.

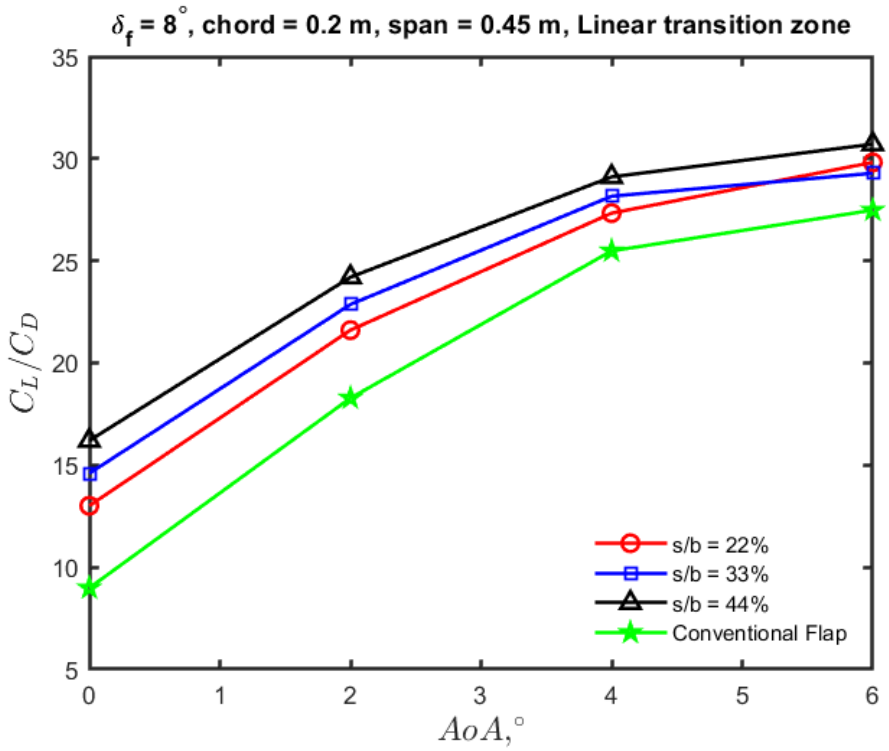

Figure 38. Aerodynamic efficiency (C_L/C_D) comparison between conventional hinged parabolic flap and continuous mold-line link flap for viscous flow conditions.

Figure 36 highlights the benefit of using continuous mold-line link (CML) flap instead of traditional hinged flap (with gap of 5mm). Even though the flap profile is parabolic, it is not able to generate the same amounts of lift as the CML flap. But there is penalty that being, CML produces more drag too. However, while the lift generated by CML and conventional flaps are quite different, the drag force is very comparable (see Figure 37). Due to which aerodynamic performance of the CML flap is much better in comparison to the conventional flap – as found in Figure 38.

3.3. Experimental validation

To validate the effects observed in the numerical study of CML and hinged parabolic flaps, experiments were conducted in Goodwin 140. We 3D printed 4 wing configurations: (1) $s/b = 22\%$; (2) $s/b = 33\%$; (3) $s/b = 44\%$; and (4) Conventional parabolic hinged flap (with 5mm gap). One of the configurations is shown in Figure 39. All the configurations were printed by the Dremel 3D printer available in the Model building Center at Virginia Tech using white Eco-ABS filament as seen in Figure 40. At once the Dremel printer can print up to a height of ~140 mm and since our wing's span is 700 mm, we printed the wings in sections.

Figure 39. Side view of the 3D printed mount placed in Goodwin 140 closed section wind tunnel.

Figure 40. Top view of a wing section being printed in Dremel 3D45 (lab 4Q).

First the wing was divided into two sections along the span, the leading-edge and the trailing-edge sections (see Figure 41). These two sections are joined using Lego-like protrusions seen in Figure 41 and Figure 42. Both of these sections are further divided into five sections along the chordwise direction. This would give us 5 leading edge pieces of size 140 mm x 140 mm (chord x span) and 5 trailing edge pieces of size 60 mm x 140 mm. Due to space constraints; the leading-edge pieces were given a box like protrusion – instead of Lego – to join them together. The 5 leading-edge and 5 trailing edge sections were glued together.

Once all the parts were printed and glued together, we would have 5 parts in total, one leading edge and 4 trailing edge parts. To smoothen the surface of all the resulting five parts, Bondo

body filler was applied to the surface and then it was sanded using 120 grit sandpaper. Finally, to get a smooth finish the surface was further sanded using 800 grit sandpaper.

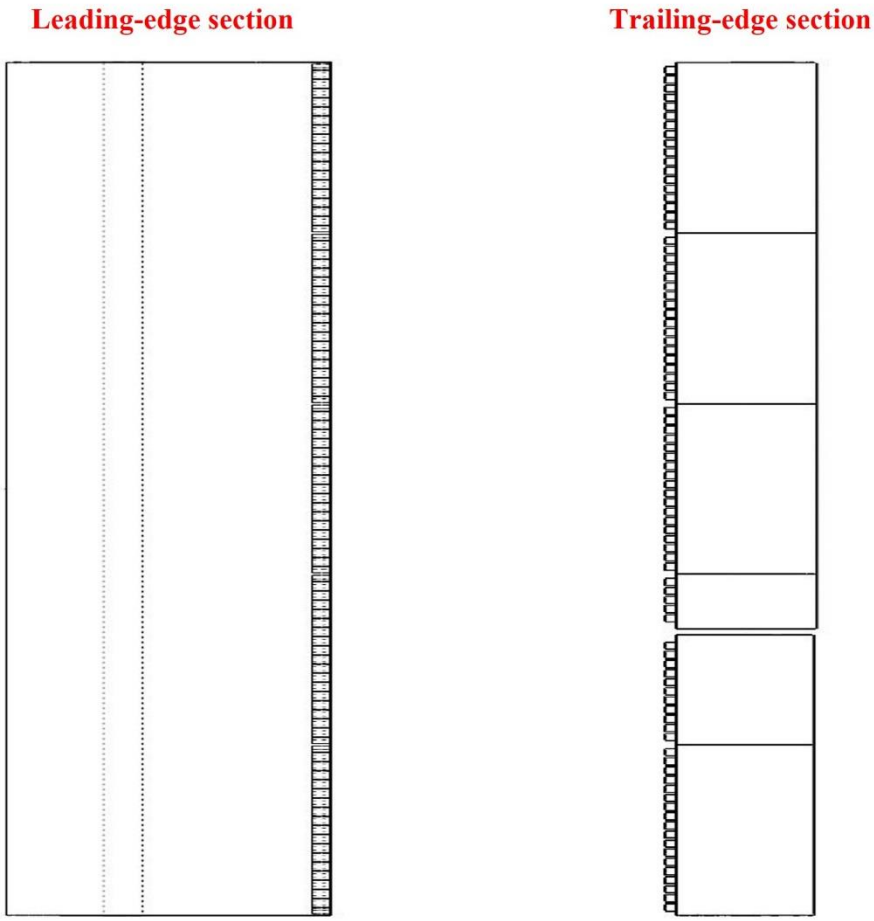

Figure 41. Top view of the conventional flap divided into two sections.

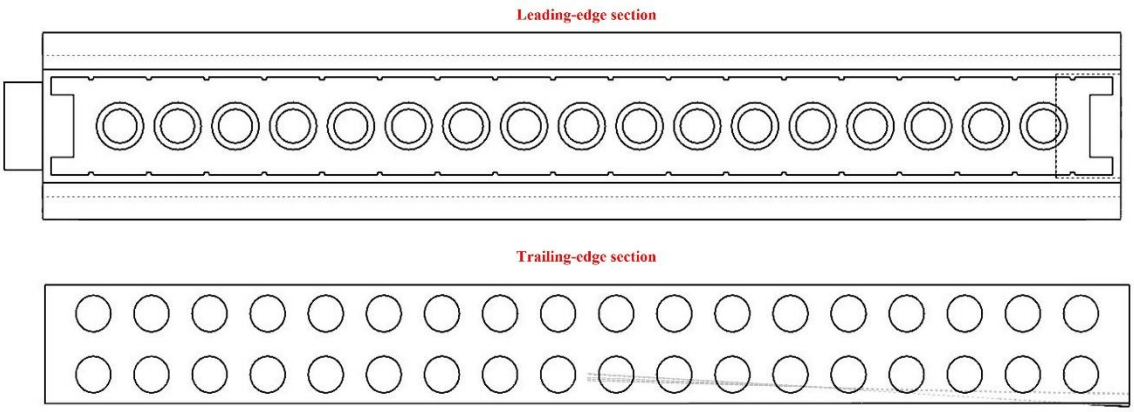

Figure 42. Sectional view of the Lego-like protrusions.

The experiments were scheduled in February but due to missing hardware in the wind tunnel, the experiments were postponed to late April. This resulted in a significant delay in the validation, and thus impacted the completion of the research and thesis.

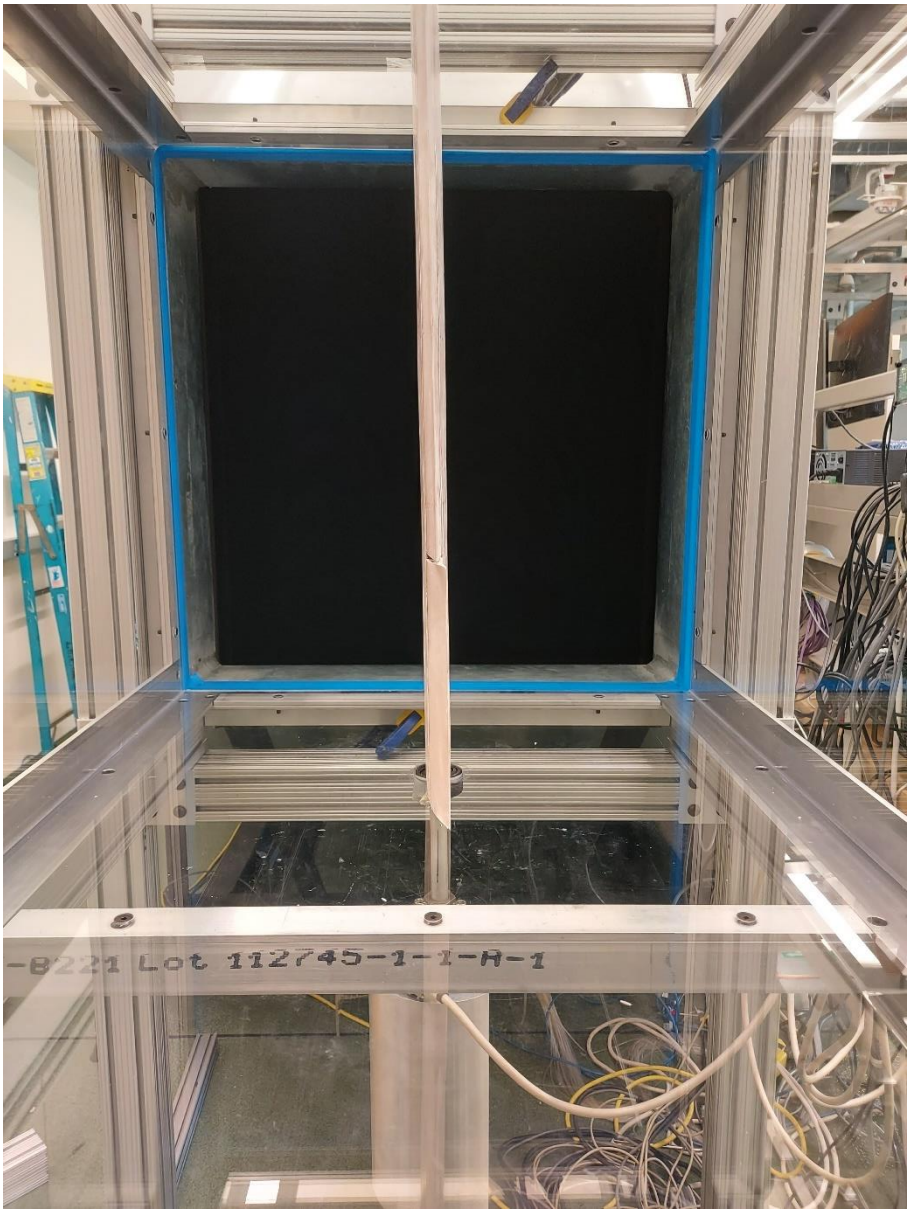

Figure 43. Back view of the 3D printed mount placed in Goodwin 140 closed section wind tunnel.

The 0.7 m subsonic open jet wind tunnel facility available at Virginia Tech (Goodwin 140) was used for the experiments. The facility houses a blower type, open circuit tunnel which is

powered by a centrifugal fan capable of flow rates up to of 15 $m3s$. The maximum fan speed is 1180 RPM with an exit flow speed of 30 ms. The open section of the wind tunnel was replaced by a closed transparent housing shown in Figure 43. The closed section had a rectangular shape of size 0.69 m x 0.69 m.

The force generated by the wing was captured using a JR3 load cell (shown in Figure 44). The load cell was mounted on a turntable (see Figure 45). A shaft that would go through the wing was clamped to the load cell. The load cell reads the loads experienced by the shaft (and hence indirectly the wing) and send it to a data file that can be loaded in MATLAB for plotting purposes. To change the angle of attack of the wing, the turntable was rotated using a MATLAB script that would send information to a DAQ that was connected to the turntable. Rotating the turntable rotates the clamped shaft and hence changes the angle at which the wing is placed in the wind tunnel.

Figure 44. JR3 45E15 load sensor with M63J bolt pattern.

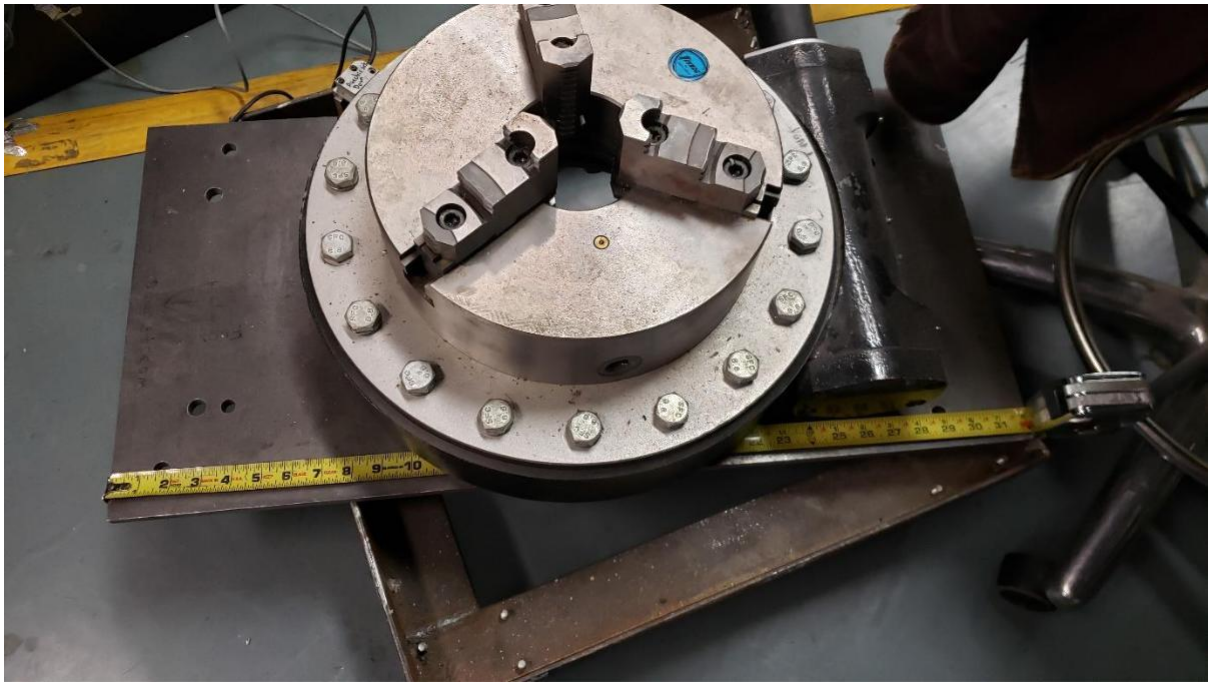

Figure 45. Rotating turntable used to change the angle of attack of the wing.

Before conducting actual experiments, the mount was tested at different fan speeds (200, 400, 600, and 800 RPM) to ensure that everything was working as intended. The data from the test run for $s/b = 33\%$ configuration is shown in Figure 46 and Figure 47. First thing to notice from these figures is that the order of magnitude of lift is one order less than drag. Also, at zero angle of attack the lift is negative which should have been positive as the flap has a positive deflection of 8°.

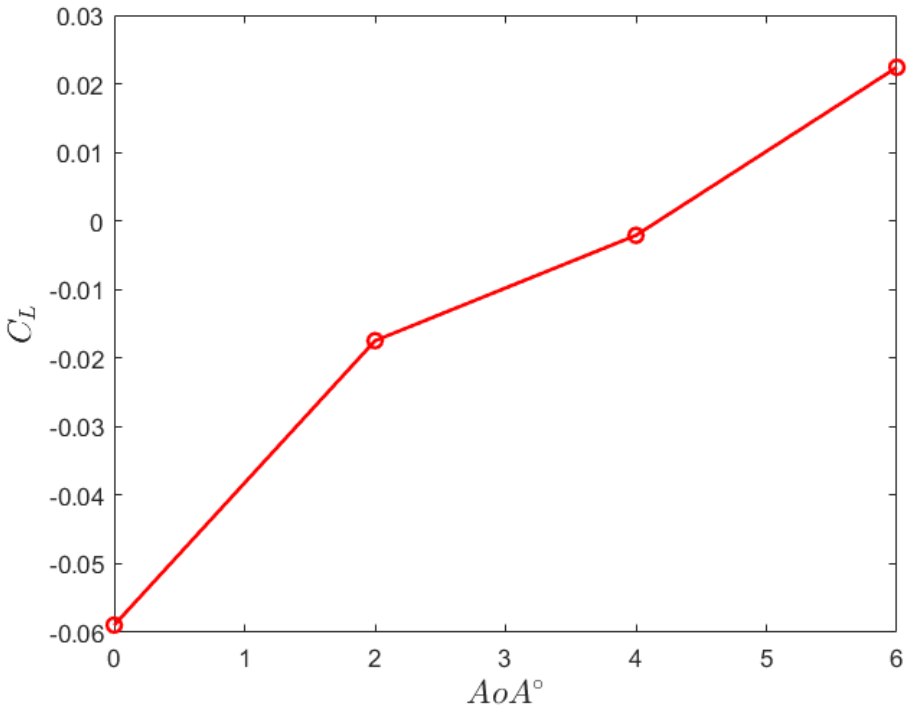

Figure 46. Variation of coefficient of lift (C_L) with angle of attack for the configuration $s/b = 33\%$.

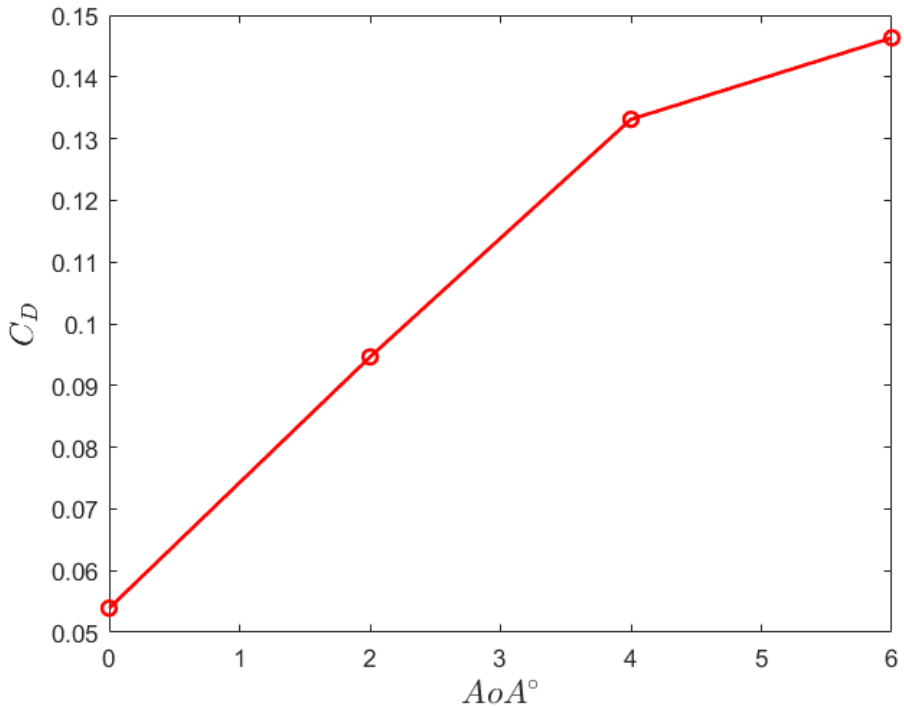

Figure 47. Variation of coefficient of lift (C_D) with angle of attack for the configuration $s/b = 33\%$.

We later found out that the mount had some unwanted compliance. The mount, when subjected to air flow, would deflect due to the forced generated by the wing. In Figure 48 and Figure 49, between different fan speed we see that the mount moves to right. We could have incorporated this deflection into the computational model by applying deflections at different angles of attack. This would have given comparable results if the wing returned to its original position – the reference position used to tare the load cell. However, in our case, the pre-run and post-run positions of the wings changed (see Figure 48 and Figure 49), which meant that the mount does not just deflect it also moves into some other resting position and hence inducing high errors in the data gathered. It was identified that the shaft that connects the wing to the load cell moves inside the stainless-steel joint used to clamp the shaft to the load cell. Hence, incorporating this movement of the shaft into the computational model is extremely difficult.

(a) Pre-run

(b) Fan speed = 200RPM

(c) Fan speed = 400RPM

(d) Fan speed = 600RPM

(e) Fan speed = 800RPM

(f) Post-run

Figure 48. Top view of the 3D printed mount placed at $\alpha = 0^o$ to the free stream in Goodwin 140 closed section wind tunnel.

(a) Pre-run

(b) Fan speed = 200RPM

(c) Fan speed = 400RPM

(d) Fan speed = 600RPM

(e) Fan speed = 800RPM

(f) Post-run

Figure 49. Top view of the 3D printed mount placed at $\alpha = 8^o$ to the free stream in Goodwin 140 closed section wind tunnel.

For the reasons discussed above and the time limitations (semester ending), we could not finish correcting the issues and gather comparable data. In future, it would be interesting to see if the data from these wind tunnel experiments replicate the findings observed in computational results.

4. Conclusion

In conclusion, we have developed a parametric curve definition that characterizes the shape of a continuous mold-line link (CML) flap. The benefits of this curve definition are that, curve parameters are controllable and the curve is smooth.

The CML flap obtained from the parametric curve definition is then tested to determine how the shape affects aerodynamic characteristics such as lift and drag. This was achieved using an ANSYS Fluent based CFD model. Two types of solvers were used, inviscid and viscous $k - \omega$ SST. Aerodynamic Results for standard NACA 0012 airfoil wing from both of these models were compared against available experimental and computational data and it was found that for low angles of attack, both models provide results that are in good agreement with available data (see Figure 17 and

Figure 20).

Additionally, the viscous model was also tested for a CML flap with linear transition zone. The aerodynamic quantities obtained from the viscous model was compared to the results published in Abdessemed, Yao, Bouferrouk and Narayan [11]. It was found that the model produced results that were in good correlation with those published in Abdessemed, Yao, Bouferrouk and Narayan [11] (see Figure 23 and Figure 24).

Initially inviscid studies were conducted as the inviscid solvers do not require intricate mesh details – like boundary layer mesh – and the solver is easy to setup. From these inviscid studies, it was found that the linear transition zone had the best aerodynamic performance (see Figure 29) which is in line with the findings published in Kamliya Jawahar, Zang and Azarpeyvand [8].

Furthermore, it was also identified that increasing the span of the transition zone initially increased the drag. But, after a certain span ratio, a dip in drag was observed (see Figure 31). The peak observed due to the dip in values, tends to shift to the right as the angle of attack was increased. This result was also seen in the aerodynamic quantities obtained from viscous simulations – Figure 34.

Viscous studies of conventional parabolic hinged flap (see Figure 8) were also conducted. The aerodynamic quantities obtained were then compared to CML flaps (see Figure 36 and Figure 38). It was found that drag produced by CML flaps was higher than conventional flaps but, very close. However, the lift produced by CML flaps was much higher when compared to conventional flap. Hence, the overall aerodynamic performance over the spectrum of angle of attacks of the CML flap was much better.

Hence, to conclude, this study is just a steppingstone to the research that is to follow. Continuous mold-line link flaps have the potential reduce noise produced by the aircrafts and at the same time increase their efficiency. And hence, it is important that we develop further understandings of its mechanisms and controllability.

5. Future Scope

In future it would be interesting to conduct experimental validation of the results obtained. This would provide further insight as to whether the dip in drag observed has some physical significance or is due to some error in model which the authors could not identify. Additionally, a coupled Computational Solid Mechanics – Computational Fluid Mechanics study can also be conducted to understand the coupled characteristics of the wing. A coupled study would help us understand the stability of the wing in different configurations and would also shed light on wings performance under dynamic conditions such as flutter.

Furthermore, over the year a lot of acoustic studies have been conducted regarding the acoustic behavior of continuous mold-line link flaps. However, only a handful of those discuss the effects of mold-line shape on the acoustics of the wing. Hence, in future an acoustic study should also be conducted to understand the effects of transition zone shape (that is controllable) on the acoustics of the wing.

References

1. Hutcheson, F. V., Brooks, T. F., and Humphreys Jr, W. M. "Noise radiation from a continuous mold-line link flap configuration," *International Journal of Aeroacoustics* Vol. 10, No. 5-6, 2011, pp. 565-588.
2. Dobrzynski, W. "Almost 40 years of airframe noise research: what did we achieve?," *Journal of aircraft* Vol. 47, No. 2, 2010, pp. 353-367.
3. Dobrzynski, W., Nagakura, K., Gehlhar, B., and Buschbaum, A. "Airframe noise studies on wings with deployed high-lift devices," *4th AIAA/CEAS Aeroacoustics Conference*. 1998, p. 2337.
4. Radeztsky, J., Ronald, Singer, B., and Khorrami, M. "Detailed measurements of a flap side-edge flow field," *36th AIAA Aerospace Sciences Meeting and Exhibit*. 1998, p. 700.
5. Storms, B. L., Takahashi, T. T., and Ross, J. C. "Aerodynamic influence of a finite-span flap on a simple wing," *SAE transactions*, 1995, pp. 1367-1376.
6. Storms, B., Jaeger, S., Hayes, J., and Soderman, P. "Aeroacoustic study of flap-tip noise reduction using continuous moldline technology," *6th Aeroacoustics Conference and Exhibit*. 2000, p. 1976.
7. Streett, C., Casper, J., Lockard, D., Khorrami, M., Stoker, R., Elkoby, R., Wenneman, W., Underbrink, J., Wenneman, W., and Underbrink, J. "Aerodynamic noise reduction for high-lift devices on a swept wing model," *44th AIAA Aerospace Sciences Meeting and Exhibit*. 2006, p. 212.
8. Kamliya Jawahar, H., Zang, N., and Azarpeyvand, M. "Aerodynamic and Aeroacoustic Performance of Spanwise Morphed Airfoils," *AIAA AVIATION 2020 FORUM*. 2020, p. 2580.
9. Pankonien, A. M., and Inman, D. J. "Aerodynamic performance of a spanwise morphing trailing edge concept," *25th International Conference on Adaptive Structures and Technologies*. 2014.
10. Ninian, D., and Dakka, S. M. "Design, development and testing of shape shifting wing model," *Aerospace* Vol. 4, No. 4, 2017, p. 52.
11. Abdessemed, C., Yao, Y., Bouferrouk, A., and Narayan, P. "Analysis of a 3D unsteady morphing wing with seamless side-edge transition," *2018 Applied Aerodynamics Conference*. 2018, p. 3178.
12. Kamliya Jawahar, H., Ai, Q., and Azarpeyvand, M. "Experimental and numerical investigation of aerodynamic performance of airfoils fitted with morphing trailing-edges," *23rd AIAA/CEAS aeroacoustics conference*. 2017, p. 3371.
13. Hunsaker, D. F., Reid, J. T., and Joo, J. J. "Geometric Definition and Ideal Aerodynamic Performance of Parabolic Trailing-Edge Flaps."
14. Barbarino, S., Bilgen, O., Ajaj, R. M., Friswell, M. I., and Inman, D. J. "A review of morphing aircraft," *Journal of intelligent material systems and structures* Vol. 22, No. 9, 2011, pp. 823-877.
15. Menter, F. R. "Two-equation eddy-viscosity turbulence models for engineering applications," *AIAA journal* Vol. 32, No. 8, 1994, pp. 1598-1605.
16. Abbott, I. H., and Von Doenhoff, A. E. *Theory of wing sections: including a summary of airfoil data*: Courier Corporation, 2012.